

PUSHING MEASUREMENT TO THE ULTIMATE STOCHASTIC  
LIMIT: THE STOCHASTIC DYNAMICS OF FLUID-COUPLED  
NANOCANTILEVERS

AFOSR FA9550-07-1-0222

FINAL REPORT

Mark Paul  
Department of Mechanical Engineering  
Virginia Tech

**Abstract**

We have developed a fundamental understanding of nanoscale fluid dynamics for fluid-based technologies with unprecedented capabilities. Using analytics and numerics we have investigated the Brownian driven, and externally driven, dynamics of micro and nanoscale elastic objects (such as cantilevers and beams) in a viscous fluid over a wide range of system parameters and for a number of experimentally important configurations. We developed an approach to compute the Brownian or externally driven dynamics using a single deterministic computation that can be performed on a personal workstation. Thermal motion is computed using the fluctuation-dissipation theorem and externally driven dynamics using transfer function theory. We quantify the effects of the cantilever and beam geometry upon their dynamics, the role of nearby bounding surfaces, the increased frequency and quality factors when using the higher flexural modes, and build a physical understanding of the fluid correlated motion of an array of elastic objects.

## **1 Computing the Stochastic and Driven Dynamics of Elastic Objects in Fluid**

The stochastic dynamics of micron and nanoscale cantilevers driven by thermal or Brownian motion can be quantified using strictly deterministic calculations. This is accomplished

| REPORT DOCUMENTATION PAGE  |                    |                         |   |  | Form Approved<br>OMB No. 0704-0188                               |  |
|--|--------------------|-------------------------|---|--|--|--|
| <p>The public reporting burden for this collection of information is estimated to average 1 hour per response, including the time for reviewing instructions, searching existing data sources, gathering and maintaining the data needed, and completing and reviewing the collection of information. Send comments regarding this burden estimate or any other aspect of this collection of information, including suggestions for reducing the burden, to the Department of Defense, Executive Services and Communications Directorate (0704-0188). Respondents should be aware that notwithstanding any other provision of law, no person shall be subject to any penalty for failing to comply with a collection of information if it does not display a currently valid OMB control number.</p> <p><b>PLEASE DO NOT RETURN YOUR FORM TO THE ABOVE ORGANIZATION.</b></p>   |                    |                         |   |  |  |  |
| 1. REPORT DATE (DD-MM-YYYY)<br>28-02-2010  |                    | 2. REPORT TYPE<br>Final |   | 3. DATES COVERED (From - To)<br>04-01-2007 to 11-30-2009               |  |  |
| <b>4. TITLE AND SUBTITLE</b><br>PUSHING MEASUREMENT TO THE ULTIMATE STOCHASTIC LIMIT - THE STOCHASTIC DYNAMICS OF FLUID-COUPLED NANOCANTILEVERS  |                    |                         |   | <b>5a. CONTRACT NUMBER</b><br>FA9550-07-1-0222                         |  |  |
|  |                    |                         |   | <b>5b. GRANT NUMBER</b><br>FA9550-07-1-0222                            |  |  |
|  |                    |                         |   | <b>5c. PROGRAM ELEMENT NUMBER</b>                                      |  |  |
| <b>6. AUTHOR(S)</b><br><br>Paul, Mark, R.  |                    |                         |   | <b>5d. PROJECT NUMBER</b>  |  |  |
|  |                    |                         |   | <b>5e. TASK NUMBER</b>   |  |  |
|  |                    |                         |   | <b>5f. WORK UNIT NUMBER</b>  |  |  |
| <b>7. PERFORMING ORGANIZATION NAME(S) AND ADDRESS(ES)</b><br>Virginia Polytechnic and State University<br>Randolph Hall (0238)<br>Blacksburg, Virginia 24061   |                    |                         |   | <b>8. PERFORMING ORGANIZATION REPORT NUMBER</b>                        |  |  |
| <b>9. SPONSORING/MONITORING AGENCY NAME(S) AND ADDRESS(ES)</b><br>Air Force Office of Scientific Research<br>875 North Randolph Street<br>Suite 325, Rm 3112<br>Arlington, VA 22203  |                    |                         |   | <b>10. SPONSOR/MONITOR'S ACRONYM(S)</b><br>AFOSR                       |  |  |
|  |                    |                         |   | <b>11. SPONSOR/MONITOR'S REPORT NUMBER(S)</b><br>AFRL-SR-AR-TR-10-0124 |  |  |
| <b>12. DISTRIBUTION/AVAILABILITY STATEMENT</b><br><br>Distribution A - Approved for Public Release   |                    |                         |   |  |  |  |
| <b>13. SUPPLEMENTARY NOTES</b>   |                    |                         |   |  |  |  |
| <b>14. ABSTRACT</b><br><p>We have developed a fundamental understanding of nanoscale fluid dynamics for fluid-based technologies with unprecedented capabilities. Using analytics and numerics we have investigated the Brownian driven, and externally driven, dynamics of micro and nanoscale elastic objects (such as cantilevers and beams) in a viscous fluid over a wide range of system parameters and for a number of experimentally important configurations. We developed an approach to compute the Brownian or externally driven dynamics using a single deterministic computation that can be performed on a personal workstation. Thermal motion is computed using the fluctuation-dissipation theorem and externally driven dynamics using transfer function theory. We quantify the effects of the cantilever and beam geometry upon their dynamics, the role of nearby bounding surfaces, the increased frequency and quality factors when using the higher flexural modes, and build a physical understanding of the fluid correlated motion of an array of elastic objects.</p> |                    |                         |   |  |  |  |
| <b>15. SUBJECT TERMS</b><br>stochastic dynamics, Brownian motion, fluctuation-dissipation theorem, quality factor, nanoscale fluid dynamics  |                    |                         |   |  |  |  |
| <b>16. SECURITY CLASSIFICATION OF:</b>   |                    |                         | <b>17. LIMITATION OF ABSTRACT</b><br><br>UU | <b>18. NUMBER OF PAGES</b><br><br>40                                   | <b>19a. NAME OF RESPONSIBLE PERSON</b><br>Mark Paul              |  |
| a. REPORT<br>n/a   | b. ABSTRACT<br>n/a | c. THIS PAGE<br>n/a     |   |  | <b>19b. TELEPHONE NUMBER (Include area code)</b><br>540-231-4758 |  |

Reset

using the fluctuation-dissipation theorem since the cantilever remains near thermodynamic equilibrium [1, 2]. As part of this research project we have extended this approach to the experimentally important case of determining the stochastic dynamics of the angle of the cantilever tip. The following discussion has been reported in Refs. [3, 4].

The autocorrelation of equilibrium fluctuations in cantilever displacement can be determined from the deterministic response of the cantilever to the removal of a step force from the tip of the cantilever (i.e. a transverse point force removed from the distal end of the cantilever). If this force  $f(t)$  is given by

$$f(t) = \begin{cases} F_0 & \text{for } t < 0 \\ 0 & \text{for } t \geq 0, \end{cases} \quad (1)$$

where  $t$  is time and  $F_0$  is the magnitude of the force, then the autocorrelation of the equilibrium fluctuations in the displacement of the cantilever tip is given directly by

$$\langle u_1(0)u_1(t) \rangle = k_B T \frac{U_1(t)}{F_0}, \quad (2)$$

where  $k_B$  is Boltzmann's constant,  $T$  is the temperature, and  $\langle \rangle$  is an equilibrium ensemble average. In our notation lower case letters represent stochastic variables ( $u_1(t)$  is the stochastic displacement of the cantilever tip) and upper case letters represent deterministic variables ( $U_1(t)$  represents the deterministic ring down of the cantilever tip due to the step force removal). The spectral properties of the stochastic dynamics are given by the Fourier transform of the autocorrelation.

The thermodynamic approach is valid for any conjugate pair of variables [5]. For example, it is common in experiment to use optical techniques to measure the angle of the cantilever tip as a function of time [6]. It has also been proposed to use piezoresistive techniques to measure voltage as a function of time [7]. The thermodynamic approach remains valid for these situations by choosing the correct conjugate pair of variables.

We have also explored the stochastic dynamics of the angle of the cantilever tip. In this case, the angle of the cantilever tip is conjugate to a step point-torque applied to the cantilever tip. If this torque is given by

$$\tau(t) = \begin{cases} \tau_0 & \text{for } t < 0 \\ 0 & \text{for } t \geq 0, \end{cases} \quad (3)$$

where  $\tau_0$  is the magnitude of the step torque, then the autocorrelation of equilibrium fluctuations in cantilever tip-angle  $\theta(t)$  is given by

$$\langle \theta_1(0)\theta_1(t) \rangle = k_B T \frac{\Theta_1(t)}{\tau_0}. \quad (4)$$

|     | $L(\mu\text{m})$ | $w(\mu\text{m})$ | $h(\mu\text{m})$ | $k(\text{N/m})$ | $k_t(\text{N-m/rad})$ | $f_0(\text{kHz})$ |
|-----|------------------|------------------|------------------|-----------------|-----------------------|-------------------|
| (1) | 197              | 29               | 2                | 1.3             | $1.6 \times 10^{-8}$  | 71                |
| (2) | 140              | 15.6             | 0.6              | 0.1             | $8.9 \times 10^{-10}$ | 38                |

Table 1: Summary of the cantilever geometries and material properties. (1) The rectangular cantilever. (2) The V-shaped cantilever used is the commercially available Veeco MLCT Type E microlever that is used in AFM [8]. The geometry is given by the cantilever length  $L$ , width  $w$ , and height  $h$ . For the V-shaped cantilever the total length between the two arms at the base is  $b = 161.64\mu\text{m}$ . The cantilever spring constant  $k$ , torsional spring constant  $k_t$ , and resonant frequency in vacuum  $f_0$  are determined using finite element numerical simulations. The cantilevers are immersed in water with density  $\rho_l = 997 \text{ kg/m}^3$  and dynamic viscosity  $\eta = 8.59 \times 10^{-4} \text{ kg/m-s}$ .

Here  $\Theta_1(t)$  represents the deterministic ring down, as measured by the tip-angle, resulting from the removal of a step point-torque. Again, the Fourier transform of the autocorrelation yields the noise spectrum.

A powerful aspect of this approach is that it is possible to use deterministic numerical simulations to determine  $U_1(t)$  and  $\Theta_1(t)$  for the precise cantilever geometries and conditions of experiment. This includes the full three-dimensionality of the dynamics which are not accounted for in available theoretical descriptions. The numerical results can be used to guide the development of more accurate theoretical models.

## 1.1 The stochastic dynamics of cantilever tip-deflection and tip-angle

The stochastic dynamics of the cantilever tip-displacement  $u_1(t)$  and that of the tip-angle  $\theta_1(t)$  yield interesting differences. Using the thermodynamic approach, insight into these differences can be gained by performing a mode expansion of the cantilever using the initial deflection required by the deterministic calculation. The two cases of a tip-force and a tip-torque result in a significant difference in the mode expansion coefficients which can be directly related to the resulting stochastic dynamics.

For small deflections the dynamics of a cantilever with a non-varying cross section are

given by the Euler-Bernoulli beam equation,

$$\mu \frac{\partial^2 U}{\partial t^2} + EI \frac{\partial^4 U}{\partial x^4} = 0, \quad (5)$$

where  $U(x, t)$  is the transverse beam deflection,  $\mu$  is the mass per unit length,  $E$  is Young's modulus, and  $I$  is the moment of inertia [9]. For the case of a cantilever where a step force has been applied to the tip at some time in the distant past the steady deflection of the cantilever at  $t = 0$  is given by

$$U(x) = -\frac{F_0}{2EI} \left( \frac{x^3}{3} - Lx^2 \right), \quad (6)$$

where  $L$  is the length of the cantilever and the appropriate boundary conditions are  $U(0) = U'(0) = U''(L) = 0$  and  $U'''(L) = -F_0/EI$ . The prime denotes differentiation with respect to  $x$ .

Similarly, the deflection of the same cantilever beam due to the application of a point-torque at the cantilever-tip is quadratic in axial distance and is given by

$$U(x) = \frac{\tau_0}{2EI} x^2, \quad (7)$$

where the appropriate boundary conditions are  $U(0) = U'(0) = U'''(L) = 0$  and  $U''(L) = \tau_0/EI$ . The angle of the cantilever measured relative to the horizontal or undisplaced cantilever is then given by  $\tan \Theta = U'(x)$ .

The mode shapes for a cantilevered beam are given by

$$\begin{aligned} \Phi_n(x) = & -(\cos \kappa L + \cosh \kappa x)(\cos \kappa L - \cosh \kappa x) \\ & + (\sin \kappa L - \sinh \kappa x)(\sin \kappa L + \sinh \kappa x), \end{aligned} \quad (8)$$

where  $n$  is the mode number, and the characteristic frequencies are given by  $\kappa^4 = \omega^2 \mu / EI$ . The mode numbers  $\kappa$  are solutions to  $1 + \cos \kappa L \cosh \kappa L = 0$  [9]. The initial cantilever displacement given by Eqs. (6) and (7) can be expanded into the beam modes

$$U(x) = \sum_{n=1}^{\infty} a_n \Phi_n(x), \quad (9)$$

with mode coefficients  $a_n$ . The total energy  $E_b$  of the deflected beam is given by

$$E_b = \frac{EI}{2} \int_0^L U''(x)^2 dx, \quad (10)$$

which is entirely composed of bending energy. The fraction of the total bending energy contained in an individual mode is given by

$$b_n = \frac{EI}{2E_b} \int_0^L (a_n \Phi_n''(x))^2 dx. \quad (11)$$

The coefficients  $b_n$  for the rectangular cantilever of Table 7 are shown in Table 2. For the case of a force applied to the cantilever tip, 97% of the total bending energy is contained in the fundamental mode and the energy contained in the higher modes decays rapidly with less than 1% of the energy contained in mode three. When a point-torque is applied to the same beam it is clear that a significant portion of the bending energy is spread over the higher modes. Only 61% of the energy is contained in the fundamental mode and the decay in energy with mode number is more gradual. The fifth mode for the tip-torque case contains more energy than the second mode for the tip-force case. Although we have only discussed a mode expansion for the rectangular cantilever, the V-shaped cantilever will exhibit similar trends since the transverse mode shapes are similar to that of a rectangular beam [10].

The variation in the energy distribution among the modes required to describe the initial deflection of the cantilever can be immediately connected to the resulting stochastic dynamics. For the deterministic calculations the initial displacement can be arbitrarily set to a small value. In this limit the modes of the cantilever beam are not coupled through the fluid dynamics. As a result, the stochastic dynamics of each mode can be treated as the ring down of that mode from the initial deflection. This indicates that the more energy that is distributed amongst the higher modes initially the more significant the ring down and, using the fluctuation-dissipation theorem, the more significant the stochastic dynamics.

The mode expansion clearly shows that the tip-torque case has more energy in the higher modes. This suggests that stochastic measurements of the cantilever tip-angle will have a stronger signature from the higher modes than measurements of cantilever tip-displacements. Using finite element simulations for the precise geometries of interest we quantitatively explore these predictions.

## 1.2 Computing the Driven Dynamics

In order to calculate the cantilever dynamics due to an external driving force we compute the cantilever's response to an appropriately chosen impulse in force. This has been done using an impulse in velocity to explore the driven dynamics of cantilevers beams of

| $n$ | $b_n$ (tip-force) | $b_n$ (tip-torque) |
|-----|-------------------|--------------------|
| 1   | 0.97068           | 0.61308            |
| 2   | 0.02472           | 0.18830            |
| 3   | 0.00315           | 0.06473            |
| 4   | 0.00082           | 0.03309            |
| 5   | 0.00030           | 0.02669            |

Table 2: The fraction of the total energy  $E_b$  contained in the first five beam modes given by the coefficients  $b_n$ . The tip-force results are for a rectangular beam that has been deflected by the application of a point force to the cantilever tip. The tip-torque results are for a rectangular beam that has been deflected by the application of a point torque to the cantilever tip. The coefficients clearly show that the tip-torque case has significantly more energy contained in the higher modes.

|     | $\langle u_1^2 \rangle^{1/2}(\text{nm})$ | $\langle \theta_1^2 \rangle^{1/2}(\text{rad})$ |
|-----|--|--|
| (1) | 5.6                                      | $5.0 \times 10^{-7}$                           |
| (2) | 20                                       | $7.0 \times 10^{-9}$                           |

Table 3: The magnitude of stochastic fluctuations in tip-deflection and in tip-angle for the rectangular (1) and V-shaped (2) cantilevers. These values were obtained from numerical simulations of the beams in vacuum.

varying geometry, near a solid wall, and including the effects of higher modes of oscillation [11]. In what follows we focus upon the dynamics of the fundamental flexural mode and allow the driving force to vary spatially given by,

$$F_d(\mathbf{x}^*, t) = \begin{cases} F_0 \delta(t) & x \leq \xi \\ 0 & x > \xi \end{cases} \quad (12)$$

where  $\mathbf{x}^* = (L, b/2, h/2)$  indicates the tip coordinates where the force is applied where  $F_0$  is a constant force. The time dependent displacement of the cantilever  $W(x, t)$  due to the application of the drive force is computed numerically. The power spectrum in terms of cantilever displacement is then given by

$$P_w(x, \omega) = \left| \hat{W}(x, \omega) \right|^2. \quad (13)$$

The power spectrum in terms of cantilever angle is found by computing the slope of  $W(x, t)$  at the region of interest to yield  $\Theta(x, t)$  and

$$P_\theta(x, \omega) = \left| \hat{\Theta}(x, \omega) \right|^2. \quad (14)$$

An advantage of this approach is that the complete spectral response over all frequency, and for all modes, is determined from a single numerical simulation. The alternative of performing many simulations at different frequencies is computationally prohibitive for these systems.

## 2 The role of cantilever geometry

In this section we report on our progress in quantifying the stochastic dynamics of a cantilever in fluid as a function of the cantilever geometry. The resulting fluid-solid interaction problem is quite complex and geometric effects can have a significant impact upon device performance. We have explored two important geometries that are commonly used: a cantilever with a rectangular cross-sectional area, and a cantilever with a V-shaped planform as shown in Fig. 1. The results of our study have been reported in detail in Refs. [3, 4].

### 2.1 Rectangular Cantilever

We have performed deterministic numerical simulations of the three-dimensional, time dependent, fluid-solid interaction problem to quantify the stochastic dynamics of a rectangular cantilever immersed in water using the thermodynamic approach previously discussed. The deterministic numerical simulations are done using a finite element approach that is described elsewhere [12, 13].

The stochastic fluctuations in cantilever tip-displacement for a rectangular cantilever in water have been described elsewhere [2, 5, 14, 15]. In the following we compare these results with the stochastic dynamics as determined by the fluctuations of the cantilever tip-angle. The geometry of the the specific micron scale cantilever we explore is given in Table 7.

The autocorrelations in equilibrium fluctuations follow immediately from the ring down of the cantilever due to the removal of a step force (to yield  $\langle u_1(0)u_1(t) \rangle$ ) or step point-torque (to yield  $\langle \theta_1(0)\theta_1(t) \rangle$ ). The autocorrelations of the rectangular cantilever are shown



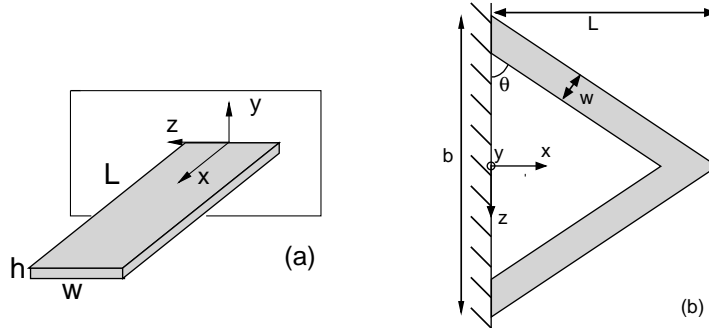


Figure 1: Schematics of the two micron scale cantilever geometries considered (not drawn to scale). Panel (a), A rectangular cantilever with aspect ratios  $L/h = 98.5$ ,  $w/h = 14.5$ , and  $L/w = 6.8$ . The cantilever is composed of silicon with density  $\rho_c = 2329 \text{ kg/m}^3$  and Youngs Modulus  $E = 174 \text{ GPa}$ . Panel (b), A V-shaped cantilever with aspect ratios  $L/h = 233$ ,  $w/h = 30$ , and  $L/w = 7.8$ . The total width between the two arms normalized by the width of a single arm is  $b/w = 10.36$ . The cantilever planform is an equilateral triangle with  $\theta = \pi/3$ . The cantilever is composed of silicon nitride with  $\rho_c = 3100 \text{ kg/m}^3$  and  $E = 172 \text{ GPa}$ . The specific dimensions for the rectangular and V-shaped cantilever are given in Table 7.

in Fig. 2. The magnitude of the noise is quantified by the root mean squared tip-angle and deflection which is listed in Table 3.

A comparison of the autocorrelations yields some interesting features. At short times  $\langle \theta_1(0)\theta_1(t) \rangle$  shows the presence of higher harmonic contributions. This is shown more clearly in the inset of Fig. 2. This further suggests that the angle autocorrelations are more sensitive to higher mode dynamics.

The Fourier transform of the autocorrelations yield the noise spectra shown in Fig. 3. In our notation the subscript of  $G$  indicates the variable over which the noise spectrum is measured:  $G_\theta$  is the noise spectrum for tip-angle and  $G_u$  is the noise spectrum for tip-displacement. The equipartition theorem of energy yields,

$$\frac{1}{2\pi} \int_0^\infty G_u(\omega) d\omega = \frac{k_B T}{k} \quad (15)$$

$$\frac{1}{2\pi} \int_0^\infty G_\theta(\omega) d\omega = \frac{k_B T}{k_t} \quad (16)$$

where  $k$  and  $k_t$  are the transverse and torsional spring constants, respectively. The curves in Fig. 3 are normalized using the equipartition result to have a total area of unity. Using this normalization the area under a peak is an indication of the amount of energy contained

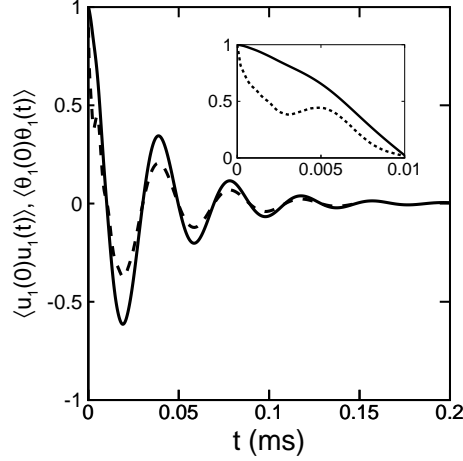


Figure 2: The normalized autocorrelation of the rectangular cantilever for tip-deflection (solid) and tip-angle (dashed). (Inset) A detailed view of the autocorrelation at short time differences to illustrate the influence of higher modes in the tip-angle measurements.

in a particular mode. Figure 3 shows only the first two modes, although the numerical simulations include all of the modes (within the numerical resolution of the finite element simulation). The energy distribution across the first two modes shows the significance of the second mode for the tip-angle dynamics.

Using a simple harmonic oscillator approximation it is straight forward to compute the peak frequency  $\omega_f$  and quality  $Q$  for the cantilever in fluid. Using a single mode approximation yields the values shown in Table 4. As expected there is a significant reduction in the cantilever frequency when compared with the resonant frequency in vacuum  $\omega_0$  and the quality factor is quite low because of the strong fluid dissipation. The values of  $\omega_f$  and  $Q$  for tip-angle and tip-displacement are nearly equal. This is expected since the displacements and angles are very small, resulting in negligible coupling between the modes. Any differences in  $\omega_f$  and  $Q$  can be attributed to using a single mode approximation.

It is useful to compare these results with the commonly used approximation of an oscillating, infinitely long cylinder with radius  $w/2$  [2, 16, 17]. The cantilever used here has an aspect ratio of  $L/w \approx 7$  and the infinite cylinder theory is quite good at predicting of  $\omega_f$  and  $Q$ .

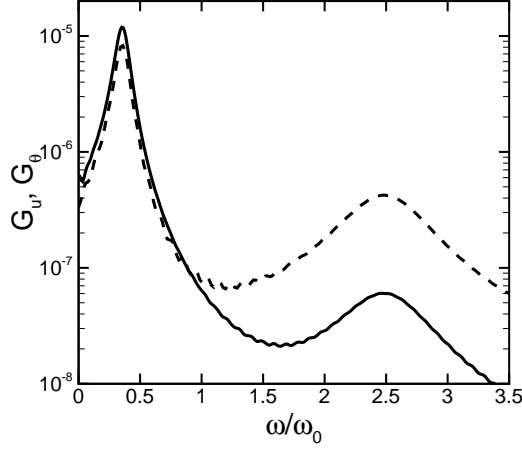


Figure 3: The noise spectra of stochastic fluctuations in cantilever tip-angle (dashed) and tip-deflection (solid) for the rectangular cantilever. The curves are normalized to have the same area, however only the first two modes are shown.

## 2.2 The stochastic dynamics of a V-shaped cantilever

We have also explored the stochastic dynamics of a V-shaped cantilever in fluid. An integral component of any theoretical model is an analytical description of the resulting fluid flow field caused by the oscillating cantilever. The deterministic finite element simulations that we performed yield a quantitative picture of the resulting fluid dynamics. Exploring the flow fields further yields insight into the dominant features that contribute to the cantilever dynamics.

As discussed earlier, for long and slender rectangular cantilevers the flow field is often approximated by that of a cylinder of diameter  $w$  undergoing transverse oscillations. This approach assumes that the fluid flow is essentially two-dimensional in the  $y - z$  plane and neglects any flow over the tip of the cantilever. Figure 4 (top) illustrates this tip flow for the rectangular cantilever using vectors of the fluid velocity in the  $x - y$  plane at  $z = 0$ . The figure is a close-up view near the tip of the cantilever. It is evident that the flow over the rectangular cantilever is nearly uniform in the axial direction leading up to the tip. However, near the tip there is a significant tip flow that decays rapidly in the axial direction away from the tip. The increasing significance of the tip flow as the cantilever geometry becomes shorter (for example, by simply decreasing  $L$ ) is not certain and remains an interesting open question. However, for the geometry used here it is clear

|     | $\omega_f/\omega_0$ | $Q$  |
|-----|---------------------|------|
| (1) | 0.35                | 3.34 |
| (2) | 0.36                | 3.26 |

Table 4: The peak frequency and quality factor of the fundamental mode of the rectangular cantilever determined by finite element simulations using the thermodynamic approach. (1) is computed using the cantilever tip-displacement due to the removal of a step force. (2) is computed using the cantilever tip-angle due to the removal of a point-torque. The frequency result is normalized by the resonant frequency in vacuum  $\omega_0$ . Using the infinite cylinder approximation with a radius of  $w/2$  the analytical predictions are  $Q = 3.24$  and  $\omega_f/\omega_0 = 0.34$ .

that this tip-flow is negligible based upon the accuracy of the analytical predictions using the two-dimensional model.

Figure 4 (bottom) illustrates the tip flow for the V-shaped cantilever, again by showing velocity vectors in the  $x - y$  plane at  $z = 0$ . The shaded region indicates the part of the cantilever where the two arms have merged. To the right of the shaded region illustrates flow off the tip and to the left indicates flow that circulates back in between the two individual arms.

In order to illustrate the three-dimensional nature of this flow, the flow field in the  $y - z$  plane is shown at two axial locations in Fig. 5. Figure 5(top) is at axial location  $x = 77\mu\text{m}$ . The two shaded regions indicate the two arms of the cantilever. Each arm is generating a flow with a viscous boundary layer (Stokes layer) as expected from previous work on rectangular cantilevers. However, the Stokes layers interact in a complicated manner near the center. It is expected that as one goes from the base of the cantilever to the tip that these fluid structures would transition from non-interacting to strongly-interacting.

Figure 5(bottom) illustrates the flow field at axial location  $x = 108.8\mu\text{m}$ , the axial location at which the two arms of the cantilever merge to form the tip region. The length of the shaded region is therefore  $36\mu\text{m}$  or twice that of a single arm shown in Fig. 5(top). For this tip region the flow field is similar to what would be expected of a single rectangular cantilever of this width.

Overall, it is clear that the fluid flow field is more complex for the V-shaped cantilever

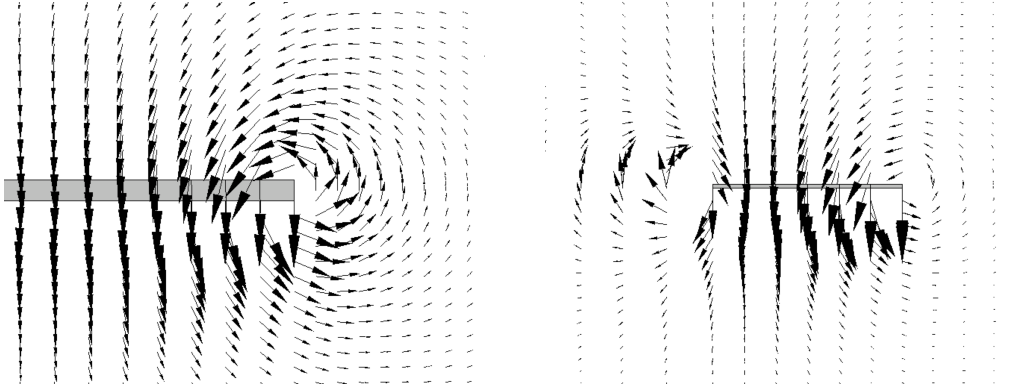


Figure 4: The fluid flow near the tip of the cantilever as illustrated by the velocity vector field calculated from finite element numerical simulations. A cross section of the  $x - y$  plane at  $z = 0$  is shown (see Fig. 1) that is a close-up view of the tip-region. The shaded region indicates the cantilever (because of the small deflections used in the simulations that cantilever does not appear to be deflected). (left) The flow field near the tip of the rectangular cantilever. This flow field is at  $t=6\mu s$  and the magnitude of the largest velocity vector shown is  $-0.3 \text{ nm/s}$ . (right) The flow field near the tip of the V-shaped cantilever. This flow field is at  $t=7.2\mu s$  and the magnitude of the largest velocity vector shown is  $-26 \text{ nm/s}$ . The shaded region indicates the tip region where the two single arms have merged. The open region to the left is where the two single arms have separated revealing the open region in the interior of the V-shaped cantilever.

than for the long and slender rectangular beam. For the V-shaped cantilever the flow is three-dimensional near the tip region where the two arms join together.

Central to the flow field dynamics are the interactions of the two Stokes layers caused by the oscillating cantilever arms. The thickness of these Stokes layers are expected to scale with the frequency of oscillation as  $\delta_s/a \sim R_\omega^{-1/2}$  where  $a$  is the half-width of the cantilever and  $R_\omega = \omega a^2/\nu$  is a frequency based Reynolds number (often called the frequency parameter). For the relevant case of a cylinder of radius  $a$  oscillating at frequency  $\omega$  the solution to the unsteady Stokes equations yields a distance of approximately  $5\delta_s$  to capture 99% of the fluid velocity in the viscous boundary layer [18]. For a single arm of the V-shaped cantilever this distance is nearly  $10\mu m$ . In comparison, the total distance between the two arms at the base is  $125\mu m$ . This separation is large enough such that the two Stokes layers have negligible interactions near the base. However, as the arms approach one another with axial distance the Stokes layers overlap and eventually merge

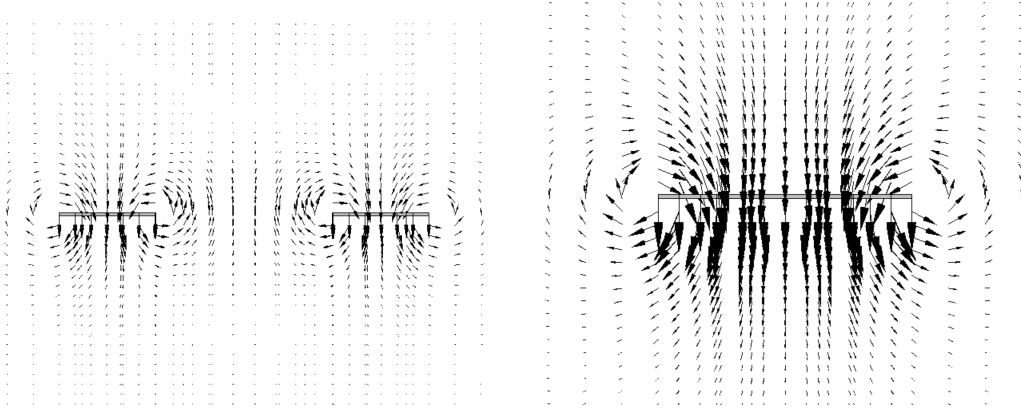


Figure 5: The fluid velocity vector field at two axial positions along the V-shaped cantilever calculated from deterministic finite element numerical simulations. Cross sections of the  $y - z$  plane are shown (see Fig. 1), the entire simulation domain is not shown and the shaded region indicates the cantilever. Both images are taken at  $t=7.2\mu\text{s}$  and the maximum velocity vector shown is  $-26\text{ nm/s}$ . (left) The  $y - z$  plane at  $x = 77\mu\text{m}$ . The skewed width of a single arm of the cantilever in this cross-section is  $18\mu\text{m}$ . The distance separating the two cantilever arms is  $36\mu\text{m}$ . (right) The  $y - z$  plane at  $x = 108.8\mu\text{m}$ . This is the point at which the two single arms join to make a continuous cross-section of width  $2w$ .

at the tip.

Despite the complicated interactions of the three-dimensional flow caused by the cantilever tip and the axial merging of the two Stokes layers, the V-shaped cantilever behaves as a damped simple harmonic oscillator. The autocorrelations in tip-angle and tip-displacement that are found using full finite element numerical simulations are shown in Fig. 6. It is again clear that the tip-angle dynamics have significant contributions from the higher modes, see the inset of Fig. 6. The area normalized noise spectra are shown in Fig. 7.

Using a simple harmonic oscillator analogy a peak frequency and a quality factor can be determined from the first mode in the noise spectra of Fig. 7. These values are given in the first two rows of Table 6. The quality of the cantilever is  $Q \approx 2$  and the peak frequency is reduced significantly,  $\omega_f/\omega_0 \approx 0.2$ , compared to the resonant frequency in the absence of a surrounding viscous fluid.

It is insightful and of practical use to determine the geometry of the equivalent rectangular beam that would yield the precise values of  $k$ ,  $\omega_f$ , and  $Q$  calculated for the V-shaped

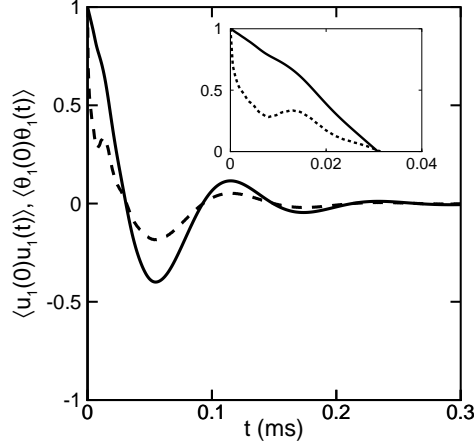


Figure 6: The normalized autocorrelation of equilibrium fluctuations in the tip-deflection  $\langle u_1(0)u_1(t) \rangle$  (solid lined) and in tip-angle  $\langle \theta_1(0)\theta_1(t) \rangle$  (dashed-line) for the V-shaped cantilever. The inset shows a close-up of the dynamics for short time differences to illustrate the influence of the higher modes in the tip-angle measurements.

cantilever from full finite-element numerical simulations. For the rectangular beam the equations are well known (c.f. Ref. [2]) and yield a unique value of length  $L'$ , width  $w'$ , and height  $h'$  as shown below,

$$k = \frac{3EI}{L'^3} = \frac{Ew'h'^3}{4L'^3}, \quad (17)$$

$$Q = \frac{m_f\omega_f}{\gamma_f} = \frac{\frac{4\rho_c h'}{\pi\rho_f w'} + \Gamma'(w', \omega_f)}{\Gamma''(w', \omega_f)}, \quad (18)$$

where the peak frequency is determined from the maximum of the noise spectrum,

$$G_u = \frac{4k_B T}{k} \frac{1}{\omega_0} \times \frac{T_0 \tilde{\omega} \Gamma''(R_0 \tilde{\omega})}{[(1 - \tilde{\omega}^2(1 + T_0 \Gamma'(R_0 \tilde{\omega}))^2 + (\tilde{\omega}^2 T_0 \Gamma''(R_0 \tilde{\omega}))^2]}. \quad (19)$$

In the above equations  $\tilde{\omega} = \omega/\omega_0$  is the normalized frequency,  $\alpha = 0.234$  is a constant factor to determine an equivalent lumped mass for a rectangular beam,  $m_f$  is the equivalent mass of the cantilever plus the added fluid mass,  $\gamma_f$  is the fluid damping,  $\Gamma$  is the hydrodynamic function for an infinite cylinder,  $\Gamma'$  is the real part of  $\Gamma$ , and  $\Gamma''$  is the imaginary part of  $\Gamma$ . Equations (28)-(18) can be solved to yield values for the unknown geometry of the equivalent rectangular beam  $L'$ ,  $w'$ , and  $h'$  which are given in Table 5. The equivalent

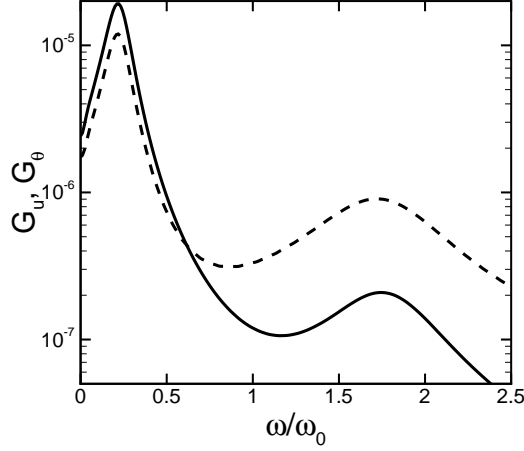


Figure 7: The noise spectra for the V-shaped cantilever as determined from the tip-displacement  $G_x$  (solid line) and from tip-angle  $G_\theta$  (dashed line). The curves are normalized to have an area of unity, with only the first two modes shown.

beam is shorter, thinner, and wider than the V-shaped cantilever. Importantly, the width of the equivalent beam is nearly twice that of a single arm of the V-shaped cantilever.

| $L'/L$ | $w'/w$ | $h/h'$ |
|--------|--------|--------|
| 0.8    | 1.9    | 0.8    |

Table 5: The geometry of the equivalent rectangular beam that yields the exact values of  $k$ ,  $\omega_f$ , and  $Q$  for the V-shaped cantilever that have been determined from full finite-element numerical simulations. The length, width, and height of the equivalent beam ( $L', w', h'$ ) are calculated using Eqs. (28)-(18) and are normalized by the values of  $(L, w, h)$  for the V-shaped cantilever given in Table 7.

These results suggest that the parallel beam approximation (PBA) [19–22] commonly used to determine the spring constant for a V-shaped cantilever may also provide a useful geometry for determining the dynamics of V-shaped cantilevers in fluid. In this approximation the V-shaped cantilever is replaced by an equivalent rectangular beam of length  $L$ , width  $2w$ , and height  $h$  to yield a simple analytical expression for the spring constant. This has been shown to be quite successful for V-shaped cantilevers that have arms that are not significantly skewed. The results of using the geometry of this approximation to determine



$\omega_f$  and  $Q$  from the two-dimensional cylinder approximation are shown on the third row of Table 6. It is clear that this is quite accurate. It is expected that these results will remain useful for cantilever geometries that do not deviate significantly from that of an equilateral triangle as studied here. An exploration of the breakdown of this approximation is possible using the methods described but is beyond the scope of the current efforts.

|              | $\omega_f/\omega_0$ | $Q$  |
|--------------|---------------------|------|
| (1)          | 0.21                | 1.98 |
| (2)          | 0.22                | 2.04 |
| $(L, 2w, h)$ | 0.19                | 1.98 |

Table 6: The peak frequency and quality factor of the fundamental mode of the V-shaped cantilever determined by finite element simulations using the thermodynamic approach. (1) is computed using the cantilever tip-displacement due to the removal of a step force. (2) is computed using the cantilever tip-angle due to the removal of a point-torque. The third line represents theoretical predictions using the geometry of an equivalent rectangular beam given by  $(L, 2w, h)$ . The frequency result is normalized by the resonant frequency in vacuum  $\omega_0$ .

### 3 The importance of nearby bounding surfaces

In practice, the cantilever is never placed in an unbounded fluid and the influence of nearby boundaries must be accounted for to provide a complete description of the dynamics. In many cases the cantilever is purposefully brought near a surface out of experimental interest in order to probe some interaction with the cantilever or to probe the surface itself. This can have a significant impact upon the performance of a device. Overall, the presence of a boundary tends to increase the viscous dissipation acting upon a cantilever causing the quality factor of the oscillations to decrease. In our research we have quantified this precisely over a wide range of experimentally relevant conditions. This work has been published in Refs. [3, 4].

To specify our discussion we will consider the situation depicted in Fig. 8 showing a cantilever a distance  $s$  from a planar boundary. In the following we study the case where

the cantilever exhibits flexural oscillations in the direction perpendicular to the boundary. However, we would like to emphasize that our approach is general and can be used to explore arbitrary cantilever orientations and oscillation directions if desired. The fluid is assumed to be unbounded in all other directions. It is well known that the presence of the boundary will influence the dynamics of the cantilever [23–25]. The result is a reduction in the resonant frequency and quality factor. This has been described theoretically for the case of a long and thin cantilever of simple geometry where the fluid dynamics have been assumed two-dimensional [26–29].

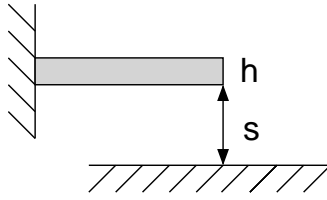


Figure 8: A schematic of a cantilever a distance  $s$  away from a solid planar surface (not drawn to scale). The cantilever undergoes flexural oscillations perpendicular to the surface.

In the following we use the thermodynamic approach with finite element numerical simulations to quantify the dynamics of the V-shaped cantilever as a function of its separation from a boundary. We have performed 8 simulations over a range of separations from 10 to  $60\mu\text{m}$  using both the tip-deflection and tip-angle formulations. The noise spectra for these simulations are shown in Fig. 9. Using the insights from our simulations of the V-shaped cantilever in an unbounded fluid we expect the relevant length scale for the fluid dynamics to be twice the width of a single arm,  $2w$ . Using the peak frequency of the V-shaped cantilever in unbounded fluid yields a Stokes length  $\delta_s = 4.14\mu\text{m}$ . Scaling the separation by the Stokes length yields  $2.5 \lesssim s/\delta_s \lesssim 15$  which covers the range from what is expected to be a strong influence of the wall to a negligible influence. Figure 9 clearly shows a reduction in the peak frequency and a broadening of the peak as the cantilever is brought closer to the boundary. In fact, for the smaller separations the peak is quite broad and the trend suggests that eventually the peak will become annihilated as the cantilever is brought closer to the boundary.

Using the noise spectra we compute a peak frequency and a quality factor for the funda-

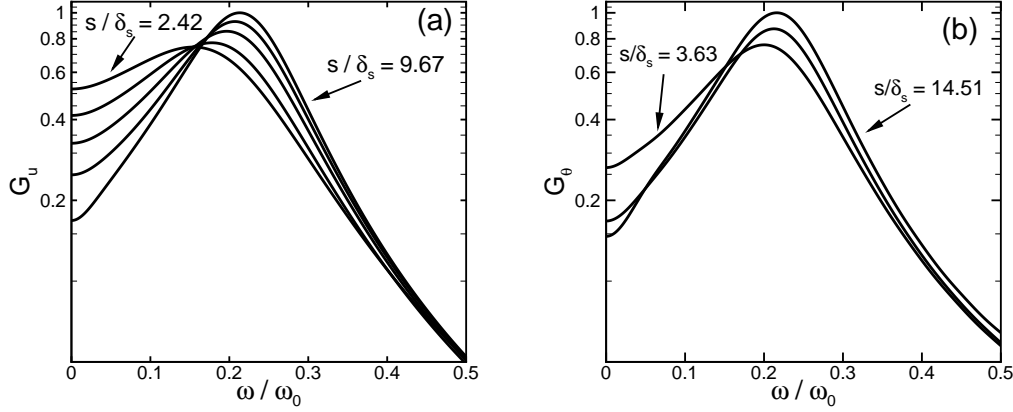


Figure 9: Panel (a) The noise spectra  $G_u$  of stochastic fluctuations in cantilever tip-deflection for separations  $s = 10, 12, 15, 20, 40\mu\text{m}$ . Panel (b) the noise spectra  $G_\theta$  of stochastic fluctuations in cantilever tip-angle for separations  $s = 15, 25, 60\mu\text{m}$ . The spectra have been normalized by the maximum value of  $G_u$  or  $G_\theta$ . The smallest and largest values of separation are labeled with all other values appearing sequentially.

mental mode as a function of separation from the boundary, which are plotted in Fig. 10. The horizontal dashed line represents the value of the peak frequency and quality factor in the absence of bounding surfaces using the two-dimensional infinite cylinder approximation [2] where the cylinder width has been chosen to be  $2w$ . It is clear from the results that for separations greater than  $s/\delta_s \gtrsim 7$  the V-shaped cantilever is not significantly affected by the presence of the boundary. However, as the separation decreases below this value the peak frequency and quality factor decrease rapidly.

The triangles in Fig. 10 represent the theoretical predictions of Green and Sader [28, 29] using a two-dimensional approximation for a beam of uniform cross-section that accounts for the presence of the boundary. We have used a width of  $2w$  in computing these theoretical predictions for comparison with our numerical results. Despite the complex and three-dimensional nature of the flow field the theory is able to accurately predict the quality factor over the range of separations explored. The frequency of the peak for the V-shaped cantilever shows some deviation from these predictions.

In general, an increase in the period of oscillation for a submerged object can be attributed to the mass of fluid entrained by the object [30]. The lower peak frequency calculated for the V-shaped cantilever using a two-dimensional solution indicates an over-prediction of

the mass loading. This can be attributed to the three-dimensional flow around the tip being neglected for this approach. It is reasonable to expect the cantilever tip to carry a smaller amount of fluid than a section of the beam body moving with the same velocity, see Fig. 4. The quality factor relates to the ratio of the mass loading and the viscous dissipation and is less sensitive to deviations incurred from the two-dimensional approximation. Despite neglecting three-dimensional flow around the cantilever tip, the two-dimensional model for the fluid flow around the V-shaped cantilever gives an accurate prediction of the peak frequency and quality factor.

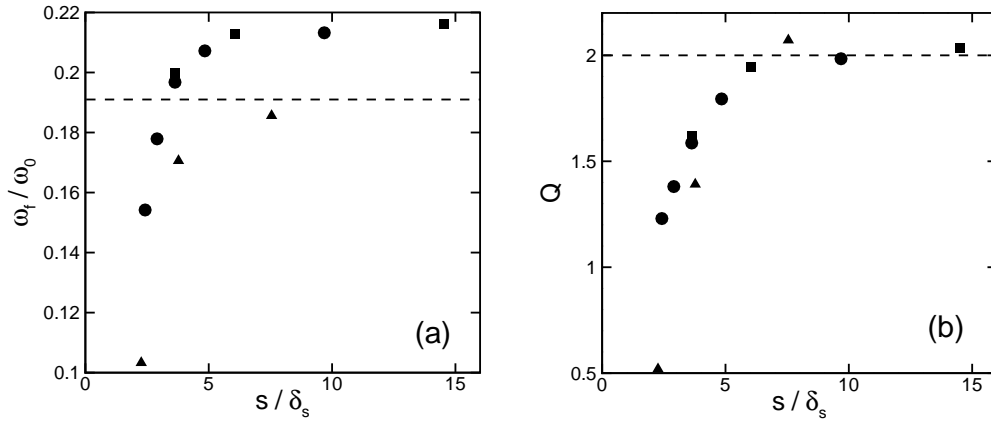


Figure 10: The variation of the peak frequency (panel (a)) and quality (panel (b)) of the fundamental mode of the V-shaped cantilever in fluid as a function of separation from a nearby wall. Results calculated using tip-deflection are circles, results using tip-angle are squares, and theoretical predictions using the results of Ref. [29] are triangles. The peak frequency and quality factor of the fundamental mode in an unbounded fluid are  $\omega / \omega_f \approx 0.19$  and  $Q \approx 2$  and are represented by the horizontal dashed line. The distance  $s$  is normalized by the Stokes length  $\delta_s$  where  $a = w$  to yield  $\delta_s = 4.14 \mu\text{m}$ .

## 4 The dynamics of doubly-clamped beams in viscous fluid: tailoring the geometry to improve quality factors

There are numerous experimental advantages to using a doubly-clamped beam as opposed to a cantilever in fluid. Important advantages include technologies for on-chip sensing and actuation that do not require bulky or complex optics. It is also anticipated that the higher

frequency of oscillation of a doubly-clamped beam, when compared to a cantilever of the same length and geometry, will lead to improved quality factors of the oscillations. In this research we have quantified this in detail for a large range of experimentally accessible parameters. Our results have been discussed in detail in Refs. [31, 32].

## 4.1 Motivation for doubly-clamped beams

There is a growing need for fast and sensitive micron and nanoscale sensors and actuators that operate in viscous fluid environments. Many important technologies are based upon the dynamics of small elastic beams in fluid [6, 33–35]. If an elastic beam is uniformly reduced in size it will become both softer (the equivalent spring constant is reduced) and faster (the fundamental frequency of oscillation increases). This advantageous trend is often exploited [35]. However, in a fluid environment the relative magnitude of viscous forces to inertial forces becomes large resulting in a dramatic reduction in the quality factor and resonant frequency of the fundamental mode of oscillation. For example, the dynamics of a nanoscale cantilever in water can be overdamped [1]. Several approaches have been proposed to overcome this difficulty including the use of the higher order beam modes [10, 11, 33, 36–38], nonlinear feedback control strategies for the external drive [39, 40], by varying the cross-sectional geometry of long-thin cantilevers that are driven externally [11], and by embedding the fluid inside the cantilever while it oscillates in vacuum [41]. However, these approaches can be difficult to implement in practice and often require sophisticated measurements and control electronics. In addition, for the strongly damped dynamics under consideration here the mode of actuation directly affects the resulting quality factor and resonant frequency (c.f. [2]). In many applications a simpler tactic is desirable to overcome the strong viscous damping. In this paper we explore the variation in beam dynamics as a function of its geometry. In particular, we quantify the stochastic dynamics of doubly-clamped beams with rectangular cross-section for a wide range of sizes and geometries including short and wide beams that are not well described by available analytical theory. Using numerical simulations for the precise conditions of experiment we quantify the Brownian driven dynamics of micron scale beams in fluid and explore the physical origins of the fluid dissipation. These results determine the effectiveness of tailoring the beam geometry to overcome the strong viscous damping.

We calculate the stochastic dynamics of the doubly-clamped beams, see Fig. 11, using the thermodynamic approach discussed in detail in Refs. [1, 2]. The approach requires

only a single deterministic calculation of the fluid dissipation that is used to compute the stochastic beam displacement via the fluctuation-dissipation theorem. For a doubly-clamped beam the deterministic calculation is the ring-down of the beam due to the removal of a step point-force applied to the center of the beam. We emphasize that the only assumptions in this result are that of classical dynamics and small deflections. Using three-dimensional, time dependent, finite element simulations for the precise geometries of interest the stochastic dynamics are computed. In particular, we calculate the autocorrelations and noise spectra of equilibrium fluctuations in the beam displacement. The basic approach has been validated both against analytics and experimental measurement [1, 2, 26, 27, 42] and also used to study the fluid-coupled motion of two atomic force microscope cantilevers [43] and two nanoscale cantilevers [1, 2]. In many situations of

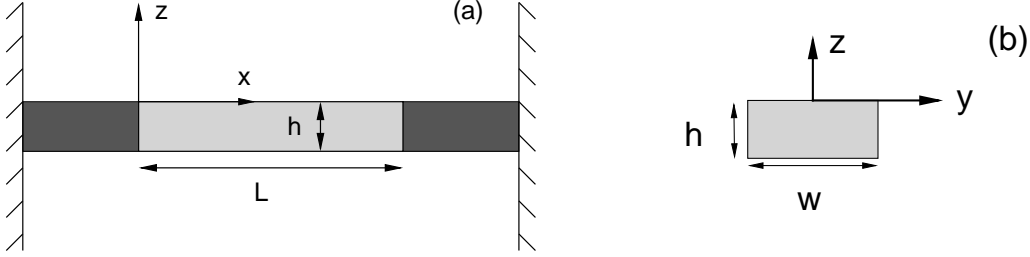


Figure 11: A schematic of a doubly-clamped beam used in the numerical simulations with length  $L$ , width  $w$ , and height  $h$  with uniform rectangular cross-section. (a) The  $x - z$  plane of the beam in fluid. The beam is supported by a rigid support of width  $w$  on each side for the short-wide geometries to minimize the effects of the bounding side walls. The beam is light grey and the two rigid supports are darker grey. (b) The  $y - z$  plane of the beam illustrating the rectangular cross-section. In our simulations the beam is immersed in room temperature water and we compute the stochastic dynamics of the fundamental flexural mode driven by Brownian motion. In the following figures the vertical displacement of the beam at  $x = L/2$  is referred to as  $z_1(t)$  for thermally induced fluctuations and  $Z_1(t)$  for the deterministic ring down simulations.

technological and scientific interest, such as atomic force microscopy, the elastic beams are long and thin  $L \gg w \gg h$  where  $L$  is the length,  $w$  is the width, and  $h$  is height of the beam. The fluid-solid interaction problem describing the motion of a waving beam in fluid is very difficult with analytical solutions available only under idealized conditions such as simple beam geometries and for small deflections [16, 17, 44, 45]. In the limit

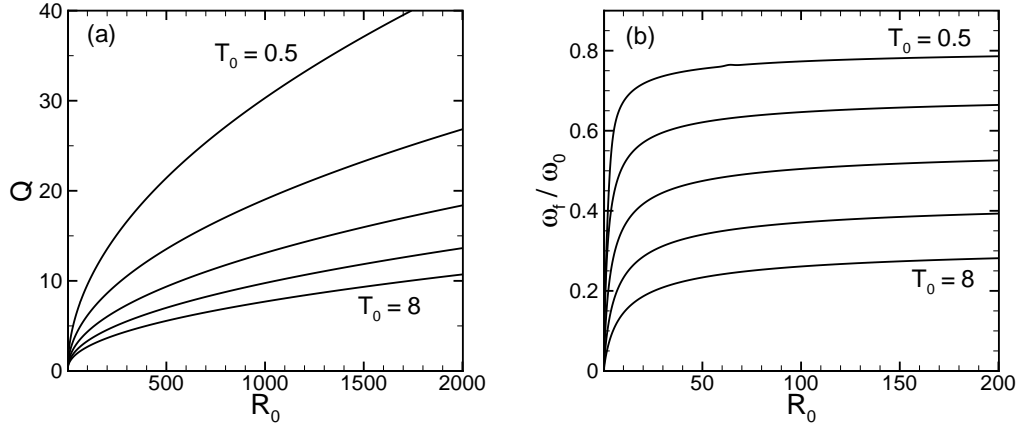


Figure 12: (a) The predicted variation of the quality factor  $Q$  for the stochastic displacement of a beam immersed in a viscous fluid with respect to the nondimensional frequency parameter  $R_0$  and mass loading parameter  $T_0$ . (b) The predicted variation of the resonant frequency in fluid  $\omega_f$  with respect to  $R_0$  and  $T_0$ . In both panels five curves are shown for  $T_0 = 0.5, 1, 2, 4, 8$ . The bounding two curves are labeled with the remaining curves in sequential order.  $R_0$  is evaluated at the resonant frequency of the beam in vacuum. The quality  $Q$  is determined by evaluating Eq. (26) at  $\omega_f$  where  $\omega_f$  is the frequency that maximizes Eq. (20).

of small beam displacements, a two-dimensional approximation for the fluid flow over the beam is often used to determine the force interactions with an Euler-Bernoulli beam. This approach has been very successful in predicting the resulting beam dynamics in a viscous fluid [16]. Furthermore, it has been shown that replacing the rectangular beam cross-section with that of a cylinder of diameter equal to the width  $w$  yields small errors on the order of several percent [17]. The flow field generated by an oscillating cylinder is well known as well as the forces acting on the surface of the cylinder [30, 46]. These approximations have led to insightful analytical expressions describing the stochastic dynamics of beams in fluid [1, 16]. However, the validity and accuracy of these expressions remain unclear for the finite beam geometries often used in experiment.

In the limit of a long and thin beam, small displacements, and using the two-dimensional approximation of an oscillating cylinder for the fluid flow, the noise spectrum of equilibrium fluctuations in displacement of the beam measured at  $x = L/2$  for the fundamental

mode is given by [1],

$$G(\omega) = \frac{4k_B T}{k} \frac{1}{\omega_0} \frac{T_0 \tilde{\omega} \Gamma_i(R_0 \tilde{\omega})}{[(1 - \tilde{\omega}^2 (1 + T_0 \Gamma_r(R_0 \tilde{\omega})))^2 + (\tilde{\omega}^2 T_0 \Gamma_i(R_0 \tilde{\omega}))^2]}, \quad (20)$$

where  $\omega$  is the frequency of oscillation,  $\tilde{\omega} = \omega/\omega_0$  is the reduced frequency,  $\omega_0$  is the resonant frequency of the fundamental mode in vacuum,  $R_0$  is the frequency parameter evaluated at  $\omega_0$ ,  $\Gamma(\omega)$  is the hydrodynamic function,  $T_0$  is the mass loading parameter,  $k_B$  is Boltzmann's constant,  $T$  is the temperature, and  $k$  is the spring constant for the fundamental mode. The frequency parameter is,

$$R_0 = \frac{\omega_0 w^2}{4\nu}, \quad (21)$$

and is a frequency based Reynolds number representing the ratio of local inertia to viscous forces where  $\nu$  is the kinematic viscosity of the fluid. In our notation, the frequency parameter  $R$  is evaluated at arbitrary frequency  $\omega$ , and  $R_f$  is evaluated at  $\omega_f$ . The mass loading parameter is

$$T_0 = \frac{\pi \rho_f w}{4 \rho_b h} \quad (22)$$

and represents the ratio of the mass of a cylinder of fluid with radius  $w/2$  to the actual mass of the beam where  $\rho_f$  is the density of the fluid, and  $\rho_b$  is the density of the beam. The hydrodynamic function for an oscillating cylinder in a viscous fluid is given by [30, 46],

$$\Gamma(\omega) = 1 + \frac{4iK_1(-i\sqrt{iR_0\tilde{\omega}})}{\sqrt{iR_0\tilde{\omega}}K_0(-i\sqrt{iR_0\tilde{\omega}})}, \quad (23)$$

where  $K_1$  and  $K_0$  are Bessel functions,  $\Gamma_r$  and  $\Gamma_i$  are the real and imaginary parts of  $\Gamma$ , respectively and  $i = \sqrt{-1}$ .

The dynamics of a beam in fluid are not precisely equivalent to that of a damped simple harmonic oscillator. For example, both the mass and damping are frequency dependent. The mass of the entrained fluid plus the mass of the beam is

$$m_f(\omega) = m_e (1 + T_0 \Gamma_r(R_0 \tilde{\omega})) \quad (24)$$

where  $m_e = \alpha m_b$  is the equivalent mass of the beam such that the kinetic energy of this mass is equal to that of the fundamental mode and  $m_b = \rho_b L w h$  is the mass of the beam. For the fundamental flexural mode of a doubly-clamped beam  $\alpha = 0.396$ . The viscous damping is

$$\gamma_f(\omega) = m_{cyl,e} \omega \Gamma_i(R_0 \tilde{\omega}) \quad (25)$$



where  $m_{cyl,e} = \alpha m_{cyl}$  is the equivalent mass of a cylinder of fluid with diameter equal to  $w$ . As the frequency of oscillation increases the magnitude of  $m_f$  decreases and the magnitude of  $\gamma_f$  increases.

The simple harmonic oscillator approximation is convenient to define commonly used diagnostics such as the quality factor  $Q$  and resonant frequency of the beam in fluid  $\omega_f$ . As a result of the frequency dependent mass and damping, the fundamental peak of the noise spectra is not well approximated as a Lorentzian for these strongly damped oscillators and care must be taken when determining  $Q$  and  $\omega_f$ . The resonant frequency in fluid  $\omega_f$  will be defined to be the frequency which maximizes the noise spectrum in Eq. (20). The quality factor  $Q$  is then defined as the ratio of energy stored by the potential and kinetic energy of the beam and fluid to the energy dissipated by viscosity per oscillation when evaluated at  $\omega_f$ . This yields

$$Q \approx \frac{m_f(\omega_f)\omega_f}{\gamma_f(\omega_f)} = \frac{T_0^{-1} + \Gamma_r(R_0\tilde{\omega}_f)}{\Gamma_i(R_0\tilde{\omega}_f)}. \quad (26)$$

Given values of the nondimensional parameters  $R_0$  and  $T_0$ , Eqs. (20) and (26) directly yield the analytical predictions for  $\omega_f$  and  $Q$ . The variation of  $Q$  and  $\omega_f$  with  $R_0$  and  $T_0$  are shown in Fig. 12 over a large range of parameters. The quality factor increases significantly as the frequency of oscillation is increased and also increases as the mass loading decreases. The resonant frequency of the beam when placed in fluid,  $\omega_f/\omega_0$ , also increases with frequency of oscillation and with a reduction in mass loading. The increase of  $\omega_f/\omega_0$  with respect to  $R_0$  is very rapid for  $R_0 \lesssim 20$  with only small changes for higher frequencies, while the dependence upon  $T_0$  results in a nearly uniform increase over the range shown. It is typical for  $R_0 \sim 1$  and  $T_0 \sim 1$  for many proposed microscale applications in water. In this case the analytics predict strongly damped dynamics with  $Q \sim 2$ . For applications that require a distinct peak to be measured this presents a significant challenge.

Using Euler-Bernoulli beam theory [9] for a doubly-clamped beam these expressions can be written as a function of geometry  $(L, w, h)$  which are often the experimentally relevant

parameters rather than  $R_0$  and  $T_0$ . The relevant expressions are,

$$\omega_0 = \frac{11.2}{\sqrt{3}} \sqrt{\frac{E}{\rho_b}} \frac{h}{L^2}, \quad (27)$$

$$k = 16E \left( \frac{h}{L} \right)^3 w, \quad (28)$$

$$R_0 = \frac{2.8}{\sqrt{3}} \frac{1}{\nu} \sqrt{\frac{E}{\rho_b}} \left( \frac{w}{L} \right)^2 h, \quad (29)$$

where  $E$  is the Youngs modulus. These expressions for  $T_0$  and  $R_0$  together with Fig. 12 suggest that  $Q$  and  $\omega_f$  increase by reducing the length, increasing the width, or increasing the height of the beam. However, the precise improvement is not clear since the available theoretical predictions are only for long and slender beams. In light of this we have performed full time-dependent and three-dimensional finite element numerical simulations [13] of a wide range of geometries to determine precisely the stochastic dynamics.

To compute the stochastic dynamics of the beams we use the approach discussed in Refs. [1, 2] and provide only the essential details necessary for our discussion. The autocorrelation of equilibrium fluctuations in beam displacement are given by the deterministic ring-down of the beam to the removal of a point step force applied at  $x = L/2$  given by

$$F(t) = \begin{cases} F_0 & \text{for } t \leq 0 \\ 0 & \text{for } t > 0 \end{cases} \quad (30)$$

where  $t$  is time, and  $F_0$  is the magnitude of the force. The value of  $F_0$  is chosen for each simulation such that the beam deflections remain small and, in this case, the results are independent of its specific value. The autocorrelation of equilibrium fluctuations in beam displacement is then given by,

$$\langle z_1(0)z_1(t) \rangle = k_B T \frac{Z_1(t)}{F_0}. \quad (31)$$

We use lower case  $z_1$  to indicate stochastic displacement, and upper case  $Z_1$  to indicate the deterministic ring-down measured at the center of the beam  $x = L/2$ . The noise spectrum of fluctuations in beam displacement is given by,

$$G(\omega) = 4 \int_0^\infty \langle z_1(t)z_1(0) \rangle \cos(\omega t) dt. \quad (32)$$

The noise spectrum is used to determine  $\omega_f$  and  $Q$  for the numerical results. The resonant frequency  $\omega_f$  is the frequency maximizing  $G(\omega)$  and the quality is given by

$$Q \approx \frac{m_f(\omega_f)\omega_f}{\gamma_f(\omega_f)} = \frac{k}{4k_B T} \omega_f^2 G(\omega_f). \quad (33)$$

The right hand side of Eq. (33) is found using  $m_f(\omega_f) = \sqrt{k/\omega_f}$  and using the peak value of the noise spectrum  $G(\omega_f)$  to determine the damping. The error in using the bulk mode spring constant, as opposed to the dynamic spring constant for the fundamental mode, is small and on the order of several percent.

In summary, the numerical procedure is the following: (i) Compute  $Z(t)$  from a deterministic simulation of the ring down of the beam due to the removal of a step force; (ii) Compute the autocorrelation of equilibrium fluctuations in displacement using Eq. (31); (iii) Compute the noise spectrum using Eq. (32); (iv) Calculate diagnostics:  $\omega_f$  is the frequency that maximizes the noise spectrum, and  $Q$  is found from Eq. (33).

We have performed extensive numerical tests on doubly-clamped beams in vacuum and in fluid to ensure the accuracy of our calculations [31]. For each geometry explored we have conducted numerical simulations over a range of spatial and temporal discretizations to ensure the convergence of our reported values for the quality factor and resonant frequency of the fundamental mode in fluid. The required spatial resolution depended significantly upon the geometry explored with the short and wide beam geometries requiring higher spatial resolution. Typically, we found that a time step  $\Delta t \lesssim P/15$  was sufficient where  $P$  is the period of the fundamental mode in vacuum. We have also been careful to choose the size of the overall simulation domain to be large enough such that the bounding walls do not affect the results. In our results, the bounding walls are always a distance of  $15\delta_s$  or greater from the beam surface where  $\delta_s = (\nu/\omega_f)^{1/2}$  is the Stokes length for the fundamental mode in fluid.

As the baseline geometry we consider a doubly-clamped beam with length  $L' = 15\mu\text{m}$ , width  $w' = 0.4\mu\text{m}$ , and height  $h' = 0.1\mu\text{m}$ . This geometry is similar to what has been recently used in experiments demonstrating thermoelastic actuation in vacuum and air [33]. Here, we are interested in the beam dynamics in a viscous fluid and use water. This geometry is referred to as case (1) in Table 7 and we consider seven additional geometries which are chosen as systematic variations of the baseline geometry  $(L', w', h')$ . Also shown in Table 7 are the aspect ratios for the different geometries to give an idea of the range of geometries used and also to give some indication of the deviation from the ideal case of a long and thin beam used in analytical predictions.

Table 8 illustrates the deviations in geometry when compared with the baseline geometry of case 1. Also included are the beam properties that can be determined independent of the fluid dynamics which include the bulk spring constant  $k$ , the frequency parameter in

vacuum  $R_0$ , and the mass loading parameter  $T_0$ . We have used finite element numerical simulations of the beams in vacuum to determine the numerical values of  $k$  and  $\omega_0$  for all of the geometries considered. Given this information one can use the analytical expressions to predict  $Q$  and  $\omega_f$  which is illustrated in Fig. 12. From Table 8 it is clear that over four orders of magnitude of spring constant, over three orders of magnitude of frequency parameter, and over a single order of magnitude of the mass loading parameter are considered by the chosen variations in geometry.

| Case | $L$ [ $\mu\text{m}$ ] | $w$ [ $\mu\text{m}$ ] | $h$ [ $\mu\text{m}$ ] | $L/w$ | $L/h$ | $w/h$ |
|------|-----------------------|-----------------------|-----------------------|-------|-------|-------|
| (1)  | 15                    | 0.4                   | 0.1                   | 37.5  | 150   | 4     |
| (2)  | 15                    | 0.8                   | 0.1                   | 18.75 | 150   | 8     |
| (3)  | 15                    | 1.2                   | 0.1                   | 12.5  | 150   | 12    |
| (4)  | 15                    | 0.4                   | 0.2                   | 37.5  | 75    | 2     |
| (5)  | 15                    | 0.4                   | 0.3                   | 37.5  | 50    | 1.33  |
| (6)  | 5                     | 0.4                   | 0.1                   | 12.5  | 50    | 4     |
| (7)  | 1                     | 0.4                   | 0.1                   | 2.5   | 10    | 4     |
| (8)  | 0.4                   | 0.4                   | 0.1                   | 1     | 4     | 4     |

Table 7: The eight geometries of doubly-clamped beams used in the numerical simulations. Case (1) is the baseline geometry and the remaining cases are variations of this geometry. The beam aspect ratios are  $L/w$ ,  $L/h$ , and  $w/h$ . The horizontal lines separate the different studies performed: the baseline geometry, variation in width, variation in height, and variation in length. The beams are composed of silicon with Young’s modulus  $E = 210$  GPa, density  $\rho_b = 3100$  kg/m<sup>3</sup> and the fluid is water with  $\rho_f = 997$  kg/m<sup>3</sup>,  $\eta = 8.56 \times 10^{-4}$  kg/ms. All simulations are performed at room temperature with  $T = 300\text{K}$ .

We first quantify the stochastic dynamics of the baseline geometry. The numerical results for the autocorrelation of equilibrium fluctuations in beam displacement are shown in Fig. 13(a), and the noise spectrum is shown in Fig. 13(b). In each figure the baseline geometry is labeled  $w'$ .

The autocorrelation curves are normalized using  $k/k_B T$  where the value of  $k$  for each case is given in Table 8. The noise spectra have been normalized using the peak value  $G(\omega_f)$ . These figures illustrate that the dynamics of this micron scale beam in water are strongly damped. The value of the quality and resonant frequency in fluid using our

| Case | $L/L'$ | $w/w'$ | $h/h'$ | $k$ [N/m] | $R_0$   | $T_0$ |
|------|--------|--------|--------|-----------|---------|-------|
| (1)  | 1      | 1      | 1      | 0.40      | 1.08    | 1.01  |
| (2)  | 1      | 2      | 1      | 0.83      | 4.55    | 2.02  |
| (3)  | 1      | 3      | 1      | 1.21      | 10.19   | 3.03  |
| (4)  | 1      | 1      | 2      | 3.19      | 2.17    | 0.51  |
| (5)  | 1      | 1      | 3      | 10.82     | 3.19    | 0.34  |
| (6)  | 1/3    | 1      | 1      | 10.92     | 10.20   | 1.01  |
| (7)  | 1/15   | 1      | 1      | 1178.95   | 231.55  | 1.01  |
| (8)  | 1/37.5 | 1      | 1      | 11413.04  | 1146.08 | 1.01  |

Table 8: The geometry variations with respect to the baseline geometry given by case (1) with  $(L', w', h')$ . Cases (2) and (3) explore increasing width, cases (4) and (5) explore increasing thickness, and cases (6)-(8) explore decreasing length. Also shown are the spring constant  $k$ , the frequency based Reynolds number in vacuum  $R_0$ , and the mass loading parameter  $T_0$ . The values of  $k$  and  $R_0$  are determined using finite element simulations.

numerical results are given in Table 9 and are  $Q = 0.80$  and  $\omega_f/\omega_0 = 0.22$ . Also shown are the predictions from analytics using Eqs. (20) and (26) which yield  $Q^\dagger = 0.68$  and  $\omega_f/\omega_0^\dagger = 0.22$ . The analytical predictions are quite accurate for the frequency drop while under predicting the quality factor for this geometry.

Next we consider the variation in the stochastic dynamics of the beam as a function of the beam width. In particular, we double and triple the beam width  $w$  while holding  $L$  and  $h$  constant. For increasing width the frequency parameter increases as  $R_0 \sim w^2$  while the mass loading parameter increases as  $T_0 \sim w$ . This has the effect of increasing the fluid inertia while simultaneously increasing the mass loading. These two counteracting effects suggest the increase in  $Q$  and  $\omega_f$  will only be moderate. The autocorrelations and noise spectra from numerical simulations are shown in Fig. 13. The autocorrelation results exhibit both positively and negatively correlated results as expected with the dynamics becoming more underdamped as the width is increased. The noise spectra clearly illustrate that the peak value shifts to higher frequency and that the peak itself becomes sharper as the width increases. For case 1, the noise spectra has significant contributions at low frequency whereas for case 3 the noise spectra has become more symmetric with a Lorentzian shape.

Values for the quality and resonant frequency in fluid from our numerical results are given

| Case | $R$    | $\omega_f/\omega_0$ | $Q$  | $Q/Q'$ | $\omega_f/\omega_0^\dagger$ | $Q^\dagger$ |
|------|--------|---------------------|------|--------|-----------------------------|-------------|
| (1)  | 0.23   | 0.22                | 0.80 | 1.0    | 0.22                        | 0.68        |
| (2)  | 1.08   | 0.24                | 1.03 | 1.29   | 0.27                        | 1.05        |
| (3)  | 2.91   | 0.29                | 1.36 | 1.71   | 0.28                        | 1.31        |
| (4)  | 1.00   | 0.46                | 1.28 | 1.61   | 0.50                        | 1.35        |
| (5)  | 2.11   | 0.66                | 2.01 | 2.52   | 0.66                        | 2.13        |
| (6)  | 4.80   | 0.47                | 1.57 | 1.97   | 0.51                        | 2.04        |
| (7)  | 164.46 | 0.71                | 6.13 | 7.69   | 0.67                        | 9.22        |
| (8)  | 885.19 | 0.77                | 5.90 | 7.40   | 0.69                        | 20.24       |

Table 9: The stochastic dynamics of the beams in fluid. Shown is the frequency based Reynolds number in fluid  $R$ , the reduction in the resonant frequency  $\omega_f/\omega_0$ , and the quality factor  $Q$ . Also shown is the improvement of the quality with respect to that of case (1) given by  $Q' = 0.8$ .  $Q^\dagger$  and  $\omega_f/\omega_0^\dagger$  are the results predicted from analytical theory using Eqs. (20) and (26).

in Table 9. When compared to the quality for the baseline geometry  $Q'$ , the increase in quality is  $Q/Q' = 1.29$  for doubling the width, and  $Q/Q' = 1.71$  for tripling the width. The quality increases with increasing width however the magnitude of the quality is small indicating that the beam dynamics remain strongly damped. The increase in the value of  $\omega_f/\omega_0$  is slightly less than what is found for  $Q$ . A comparison of our numerical values of  $\omega_f$  and  $Q$  with the analytical predictions of Eqs. (20) and (26) are shown in Fig. 14. The circles are the results from our numerical simulations and the dashed line is the analytical prediction where  $\xi = w/w'$  and  $w'$  is the width of the baseline geometry. It is clear that that the analytical predictions remain quite accurate over this range. This includes case 3 where  $L/w \approx w/h \approx 12$  and  $L/h \gg 1$ . Figure 14 indicates that the magnitude of the increase in quality with increasing width is quite moderate. Furthermore, the increase in  $\omega_f$  is quite small and becomes nearly flat at  $\omega_f/\omega_0 \approx 0.24$  for  $\xi \gtrsim 2$ .

Next we consider the variation in beam dynamics as the height is increased. We consider the cases where  $h$  is doubled and tripled while the  $L$  and  $w$  are held constant. As the height is increased the frequency parameter increases as  $R_0 \sim h$  whereas the mass loading parameter decreases as  $T_0 \sim h^{-1}$ . These two effects both contribute to increasing  $Q$  and  $\omega_f$ . The normalized autocorrelations and noise spectra from our numerical simulations are shown in Fig. 15. The results clearly indicate an increasing value of both  $\omega_f$  and  $Q$

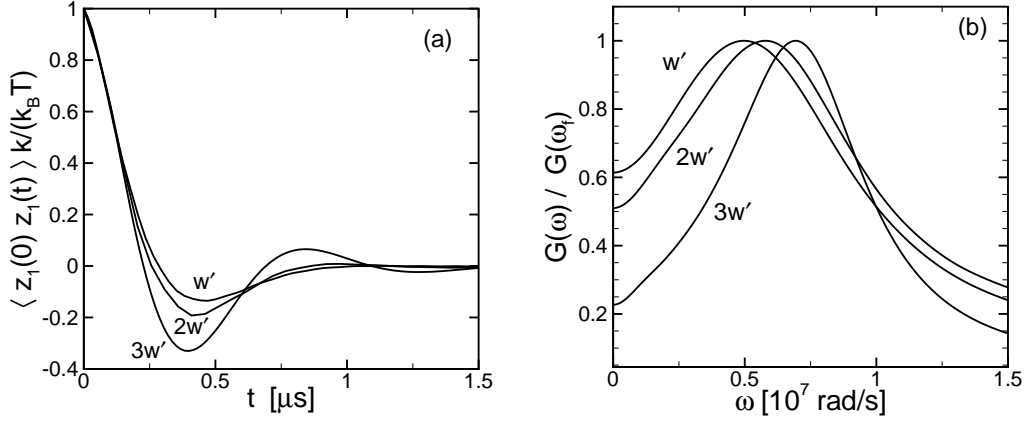


Figure 13: The autocorrelations and noise spectra of equilibrium fluctuations in beam displacement as a function of beam width from numerical results: case 1 ( $w'$ ), case 2 ( $2w'$ ), case 3 ( $3w'$ ). (a) The autocorrelations, the results have been normalized using  $k/(k_B T)$  for each case. (b) The noise spectra, the results have been normalized by the peak value for each case,  $G(\omega_f)$ .

and numerical values are given in Table 9. The relative increase in quality is  $Q/Q' = 1.61$  when the height is doubled, and  $Q/Q' = 2.52$  when the height is tripled. The increase in  $\omega_f/\omega_0$  follows a similar trend.

A comparison of our numerical results with the predictions of theory is shown in Fig. 14 using  $\xi = h/h'$ . The square symbols are the numerical results and the solid line is the analytical prediction. It is clear that the increases in  $Q$  and  $\omega_f$  are much larger for variations in height when compared to what was found for increases in beam width. The analytical predictions remain quite accurate and insightful over the range of aspect ratios explored by varying the beam height. We highlight that this includes case 5 where  $w/h \approx 1$ .

The last case we consider is decreasing the beam length while holding the width and height constant. In this case the frequency parameter increases rapidly as  $R_0 \sim L^{-2}$  whereas  $T_0$  remains constant. The autocorrelations and noise spectra are shown in Fig. 16 which illustrate a significant increase in resonant frequency and quality. From Fig. 16(a) the results for the most extreme geometry explored,  $L'/37.5$ , clearly show the influence of higher harmonics. The numerical values of  $Q$  and  $\omega_f$  from our numerical results are given Table 9. For case 8 where  $L/L' = 37.5$  the increase in quality is  $Q/Q' = 7.4$  and the reduction of the resonant frequency when compared to its value in vacuum is

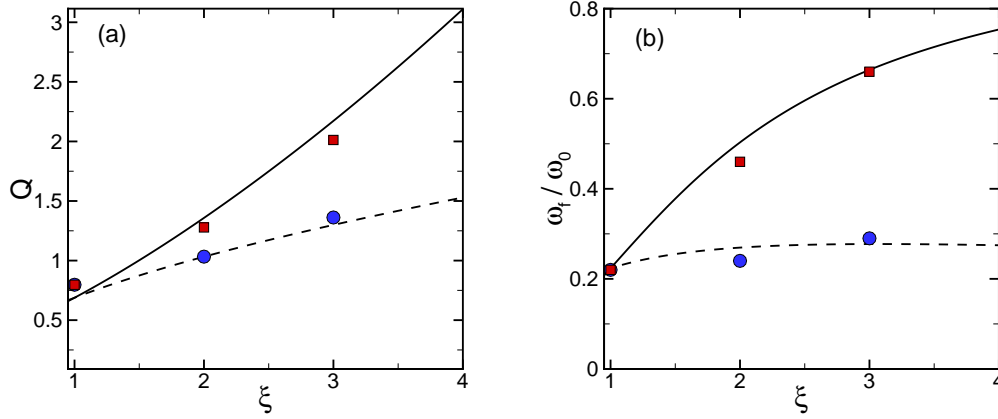


Figure 14: (color) Comparison of numerical results with analytical predictions for  $Q$  and  $\omega_f$  as a function of width  $w$  and height  $h$ . The circles (blue) are for increasing width and the squares (red) are for increasing height. The solid line is the analytical prediction for increasing width and the dashed line is the analytical prediction for increasing height. To place all values on a single plot  $\xi = w/w'$  for the varying width results and  $\xi = h/h'$  for the varying height results.

$\omega_f/\omega_0 = 0.77$  indicating significant changes are possible by changing the beam length.

The analytical predictions given in Table 9 show significant deviations from our numerical results. This is also illustrated in Fig. 17 where the triangles are the numerical results and the solid lines are the analytical predictions. For case 6 ( $L/w = 12.5$ ) the analytical predictions are quite accurate. However, for case 7 ( $L/w = 2.5$ ), and case 8 ( $L/w = 1$ ) the analytical predictions over predict  $Q$  and under predict  $\omega_f/\omega_0$ . The approximation of using the fluid flow from an infinite two-dimensional oscillating cylinder is no longer well justified. The numerical results suggest the presence of additional modes of fluid dissipation that are not captured in the two-dimensional theory.

To explore this further we quantify the fluid motion around the beam in the deterministic numerical simulations where the beam rings down upon the removal of a step force. Figures 18 and 19 illustrate the magnitude of the fluid velocity in the transverse  $u_z$  and axial  $u_x$  directions, respectively. The velocities are plotted along a line beginning at  $(0.0, 0.0, 0.01\mu\text{m})$  and ending at  $(L, 0.0, 0.01\mu\text{m})$  for all cases. In our notation the fluid velocity in the  $(x, y, z)$  directions is  $(u_x, u_y, u_z)$ , see Fig. 11 for the definition of the coordinate directions  $(x, y, z)$ . The velocities are shown at the time when the velocity of the



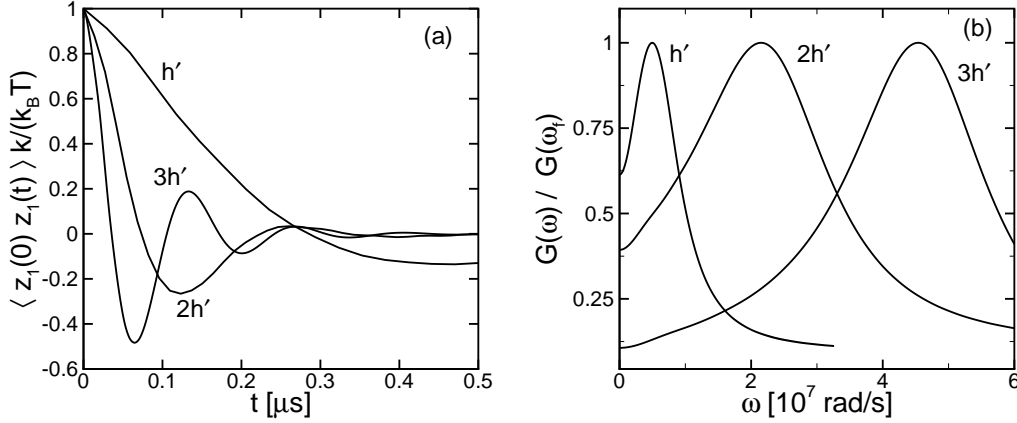


Figure 15: The autocorrelations and noise spectra as a function of beam height from numerical results: case 1 ( $h'$ ), case 4 ( $2h'$ ), case 5 ( $3h'$ ). (a) The normalized autocorrelations. (b) The normalized noise spectra.

beam is at its maximum value which occurs when the center of the beam crosses  $z = 0$  the first time during its ring down. The maximum value of  $u_z$  at this time is labeled  $u_0$  and is used to normalize both the transverse and axial velocities. The axial direction is normalized by the length so that all cases can be represented on the same figure.

Figure 18 shows the transverse fluid velocity  $u_z$  for cases 1-8. The baseline geometry (dashed line) and cases 2-7 (solid lines) collapse onto a single curve with a shape similar to that of the fundamental mode of a doubly-clamped beam. Case 8 differs significantly with a much sharper peak indicating that its dynamics are quite different which is expected since this geometry is substantially different than the others.

Figure 19(a) illustrates the normalized axial velocities  $u_x$  as the beam width and height are varied. In the approximation of a two-dimensional flow the axial velocity is identically zero and any deviations from this in the numerical results indicate fluid dynamics not considered in the analytical predictions. The bimodal shape of the curves is expected from the symmetry of the fundamental mode. For  $x > L/2$  the axial fluid velocity is positive and for  $x < L/2$  it is negative. The baseline geometry is shown as the dashed line and has a negligible axial fluid velocity. At its maximum value it is only  $\sim 2.5\%$  of the maximum transverse velocity  $u_0$ . A similar trend is found for cases 2-5. As the width or height is increased the relative magnitude of the axial velocities increase. It is expected that if larger values of the width or height were computed the axial velocities

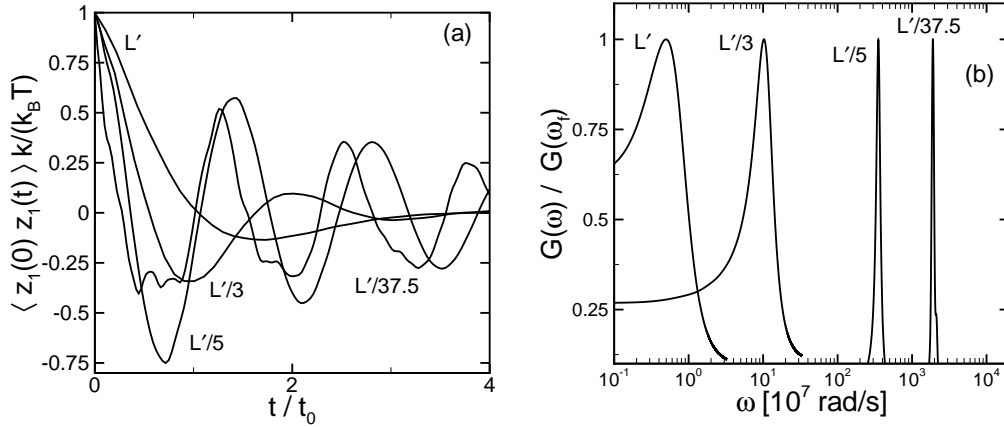


Figure 16: The autocorrelations and noise spectra as a function of beam length from numerical results: case 1 ( $L'$ ), case 6 ( $L'/3$ ), case 7 ( $L'/5$ ), case 8 ( $L'/37.5$ ). (a) The normalized autocorrelations. (b) The normalized noise spectra.

would become significant and at this point the analytical predictions would show large deviations.

Figure 19(b) shows the relative value of the axial velocities as the length of the beam is decreased. The baseline geometry is included for reference as the dashed line. It is clear that the axial velocities are now quite significant and range from 10% to 40% of  $u_0$ . The axial velocities do not vanish at  $x = 0, L$  for cases 7 and 8 because these beams are held by rigid supports, see Fig. 11, and the lateral side walls of the numerical domain are distant. The axial velocities result in fluid dissipation not accounted for in the two-dimensional theory and contribute significantly to the lower values of  $Q$  found in the numerical simulations. Furthermore,  $\omega_f$  from the numerical simulations are larger than the analytical predictions. The added mass in the simulations are smaller than the predicted values and this reduction is a direct result of the three-dimensionality of the fluid flow. The maximum value of the relative axial velocity does not follow a monotonic trend with  $L$  because as the length becomes small the precise nature of the beam dynamics vary in a complicated manner which directly affects the fluid motion and therefore the fluid dissipation. In fact, the smallest beam  $L'/37.5$  has an aspect ratio of  $L/w = 1$  and is better described as a plate undergoing complicated dynamics as indicated by the presence of higher mode effects in Fig. 16(a). Overall, our results suggest that the relative magnitude of the axial velocity can be used to indicate the applicability of the two-dimensional theory.

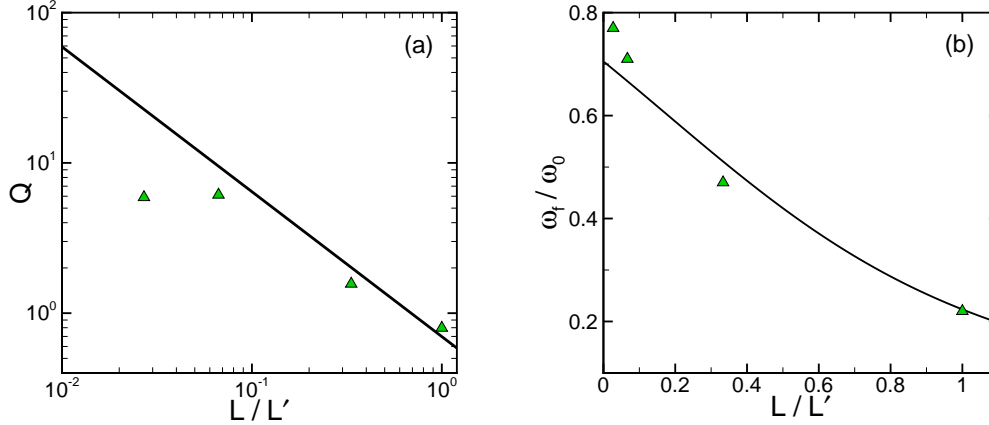


Figure 17: (color) The variation of the quality  $Q$ , panel (a), and of the resonant frequency in fluid  $\omega_f/\omega_0$ , panel (b), by decreasing the length  $L$  of the beam relative to the value of case (1) given by  $L'$ . The triangles are the results from numerical simulation and the solid line is the analytical prediction.

In many microscale technologies the ability to sense small forces is important and therefore a small spring constant is desirable. In light of this, the improved performance, as measured by increased values of  $Q$  and  $\omega_f$  with increasing  $w$ , increasing  $h$  or decreasing  $L$  all come at the price of reduced force sensitivity. Using Eq. (28) to estimate  $k$  yields its dependence upon geometry and the magnitude of the improved performance follows the same trend as increasing  $k$ . Overall, these tradeoffs would need to be balanced in a particular application.

The stochastic dynamics of micron and nanoscale elastic beams can be directly quantified using deterministic numerical computations for the precise geometries and conditions of experiment. We have shown that the geometry of doubly-clamped beams can be tailored to overcome the strong fluid damping that occurs for small scale systems in a viscous fluid. Our numerical exploration has been used to build physical insights into the stochastic dynamics and to place realistic bounds upon the applicability of the two-dimensional theory. Overall, we find that the two dimensional theory is quite accurate far beyond what may have been expected based upon the underlying assumptions. When deviations do occur a significant factor are fluid velocities in the axial direction resulting in increased dissipation and a lower added mass. It is anticipated that these results will be useful in guiding the development of future experiments by providing the basis for predictions that cover a wide range of geometries. Furthermore, our results provide insight into the development

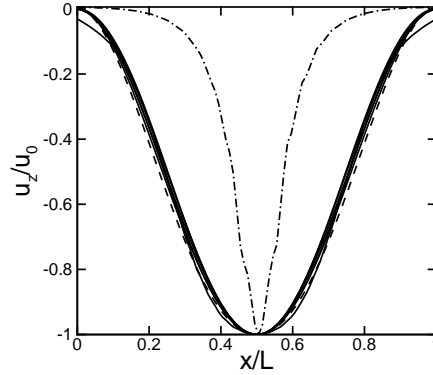


Figure 18: The transverse fluid velocity  $u_z$  for cases 1-8 along the line beginning at  $(0.0, 0.0, 0.01 \mu\text{m})$  and ending at  $(L, 0.0, 0.01 \mu\text{m})$  from the deterministic numerical simulations where the beam velocity is at its maximum value. The baseline geometry is shown as the dashed line, cases 2-7 are the solid lines, and case 8 is the dash-dot line.

of accurate theoretical models valid for the finite geometries used in experiment.

## 5 Executive Summary

We have developed analytical and theoretical techniques to quantify the stochastic and externally driven dynamics of elastic objects in a viscous fluid for the precise conditions of experiment. These techniques allow the quantification of future designs aiming to exploit the dynamics of micro and nanoscale devices in fluid.

This project provided support for the following graduate research. The theses are available to the public in digital form from the University Library at Virginia Tech ([www.lib.vt.edu](http://www.lib.vt.edu)). The specific thesis details are given below:

- Margarita Villa, Masters Thesis, Tailoring the geometry of micron scale resonators to overcome viscous damping, Virginia Tech, (2009).
- Matthew Clark, PhD Dissertation, The driven and stochastic dynamics of micro and nanoscale cantilevers in viscous fluid and near a solid boundary, Virginia Tech, (2008).

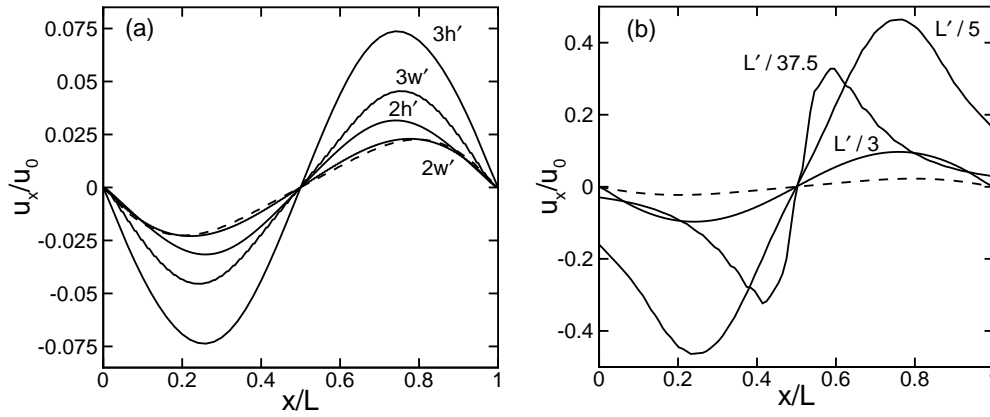


Figure 19: The normalized axial velocity from numerical simulation. (a) The axial velocity found when varying the width and height of the baseline geometry. (b) The axial velocity found when decreasing the length of the baseline geometry. The results for the baseline geometry are given by the dashed line. The axial velocities are computed along a line in the  $x$ -direction with origin  $(0,0,0.01\mu\text{m})$  and end-point  $(L,0,0.01\mu\text{m})$ , see Fig. 11 for definitions of coordinate directions. The velocity is normalized by  $u_0$  for each case where  $u_0$  is the maximum transverse velocity which occurs at  $x = L/2$ . The abscissa is normalized by the length  $L$  for each case.

- Carlos Carvajal, Masters Thesis, The fluid coupled motion of micro and nanoscale cantilevers, Virginia Tech, (2007).

This project has supported the following journal articles that are available in the open literature.

- M.M. Villa and M.R. Paul, Stochastic dynamics of micron-scale doubly clamped beams in a viscous fluid, *Physical Review E*, **69**, 056314, (2009).
- M.T. Clark and M.R. Paul, The stochastic dynamics of rectangular and V-shaped atomic force microscope cantilevers in a viscous fluid and near a solid boundary, *Journal of Applied Physics*, **103**, 094910, (2008).

## References

- [1] M. R. Paul and M. C. Cross. Stochastic dynamics of nanoscale mechanical oscillators in a viscous fluid. *Physical Review Letters*, 92(23):235501, 2004.
- [2] M.R. Paul, M.T. Clark, and M.C. Cross. The stochastic dynamics of micron and nanoscale elastic cantilevers in fluid: fluctuations from dissipation. *Nanotechnology*, 17:4502–4513, 2006.
- [3] M. T. Clark and M. R. Paul. The stochastic dynamics of rectangular and V-shaped atomic force microscope cantilevers in a viscous fluid and near a solid boundary. *J. Appl. Phys.*, 103:094910, 2008.
- [4] M. T. Clark. *The driven and stochastic dynamics of micro and nanoscale cantilevers in viscous fluid and near a solid boundary*. PhD thesis, Virginia Polytechnic and State University, 2008.
- [5] M. R. Paul and M. C. Cross. Stochastic dynamics of nanoscale mechanical oscillators immersed in a viscous fluid. *Physical Review Letters*, 92(23):235501, 2004.
- [6] R. Garcia and R. Perez. Dynamic atomic force microscopy methods. *Surface Science Reports*, pages 197–301, 2002.
- [7] J. L. Arlett, J. R. Maloney, B. Gudlewski, M. Muluneh, and M. L. Roukes. Self-sensing micro- and nanocantilevers with attonewton-scale force resolution. *Nano Lett.*, 6(5):1000–1006, 2006.
- [8] Veeco Probes, [www.veecoprobes.com](http://www.veecoprobes.com).
- [9] L. D. Landau and E. M. Lifshitz. *Theory of elasticity*. Butterworth-Heinemann, 1959.
- [10] R.W. Stark, T. Drobek, and W.M. Heckl. Thermomechanical noise for a free v-shaped cantilever for atomic force microscopy. *Ultramicroscopy*, 86:207–215, 2001.
- [11] S. Basak, A. Raman, and S.V. Garimella. Hydrodynamic loading of microcantilevers vibrating in viscous fluids. *J. Appl. Phys.*, 99:114906, 2006.
- [12] H. Q. Yang and V. B Makhijani. A strongly-coupled pressure-based CFD algorithm for fluid-structure interaction. *AIAA-94-0179*, pages 1–10, 1994.

- [13] ESI Group. CFD ACE+ Advanced Multiphysics Software, Paris France.
- [14] J. W. M. Chon, Mulvaney P., and J. E. Sader. Experimental validation of theoretical models for the frequency response of atomic force microscope cantilever beams immersed in fluids. *Journal of Applied Physics*, 87(8):3978–3988, 2000.
- [15] M. T. Clark and M. R. Paul. The stochastic dynamics of an array of atomic force microscopes in a viscous fluid. *International Journal of Nonlinear Mechanics*, 2006.
- [16] J. E. Sader. Frequency response of cantilever beams immersed in viscous fluids with applications to the atomic force microscope. *J. Appl. Phys.*, 84(1):64–76, 1998.
- [17] E. O. Tuck. Calculation of unsteady flows due to small motions of cylinders in a viscous fluid. *J. Eng. Math*, 3(1):29–44, 1969.
- [18] C. Carvajal and M. R. Paul. Unpublished. Unpublished.
- [19] T. R Albrecht, S. Akamine, and C. F. Carver, T. S. and Quate. Microfabrication of cantilever styli for the atomic force microscope. *J. Vac. Sci. Technol. A*, 8(4):3386–3396, 1990.
- [20] J. E. Sader. Parallel beam approximation for v-shaped atomic force cantilevers. *Rev. Sci. Instrum.*, 66(9):4583–4587, 1995.
- [21] J. E. Sader and L. White. Theoretical-analysis of the static deflection of plates for atomic-force microscope applications. *J. Appl. Phys*, 74(1):1–9, 1993.
- [22] H.J. Butt, P. Siedle, K. Seifert, K. Fendler, T. Seeger, E. Bamberg, A.L. Weisenhorn, K. Goldie, and A. Engel. Scan speed limit in atomic force micropscopy. *J. Microsc.*, 169(1):75–84, 1993.
- [23] F. Benmouna and D. Johannsmann. Hydrodynamics interaction of AFM cantilevers with solid walls: An investigation based on AFM noise analysis. *Eur. Phys. J. E*, 9:435–441, 2002.
- [24] I. Nnebe and J. W. Schneider. Characterization of distance-dependent damping in tapping-mode atomic force microscopy force measurements in liquid. *Langmuir*, 20:3195–3201, 2004.

- [25] C. Harrison, E. Tavernier, O. Vancauwenberghe, E. Donzier, K. Hsu, A.R.H. Goodwin, F. Marty, and B. Mercier. On the response of a resonating plate in a liquid near a solid wall. *Sensor and Actuators A*, 134:414–426, 2007.
- [26] R. J. Clarke, S. M. Cox, P. M. Williams, and O. E. Jensen. The drag on a microcantilever oscillating near a wall. *J. Fluid Mech.*, 545:397–426, 2005.
- [27] R. J. Clarke, O. E. Jensen, J. Billingham, A. P. Pearson, and P. M. Williams. Stochastic elastohydrodynamics of a microcantilever oscillating near a wall. *Phys. Rev. Lett.*, 96:050801, 2006.
- [28] C. P. Green and J. E. Sader. Small amplitude oscillations of a thin beam immersed in a viscous fluid near a solid surface. *Phys. Fluids*, 17:073102, 2005.
- [29] C. P. Green and J. E. Sader. Frequency response of cantilever beams immersed in viscous fluids near a solid surface with applications to the atomic force microscope. *J. Appl. Phys.*, 98:114913, 2005.
- [30] G. G. Stokes. On the effect of the internal friction of fluids on the motion of pendulums. *Trans. Cambridge Philos. Soc.*, 9:8, 1851.
- [31] M.M. Villa and M.R. Paul. Stochastic dynamics of micron-scale double clamped beams in a viscous fluid. *Phys. Rev. E*, 79:056314, 2009.
- [32] M.M. Villa. Tailoring the geometry of micron scale resonators to overcome viscous damping. Master’s thesis, Virginia Polytechnic and State University, 2009.
- [33] I. Bargatin, I. Kozinsky, and M.L. Roukes. Efficient electrothermal actuation of multiple modes of high-frequency nanoelectromechanical resonators. *Applied Physics Letters*, 90:093116, 2007.
- [34] S.S. Verbridge, L.M. Bellan, J.M. Parpia, and H.G. Craighead. Optically driven resonance of nanoscale flexural oscillators in liquid. *Nano Lett.*, 6(9):2109–2114, 2006.
- [35] K. L. Ekinici and M. L. Roukes. Nanoelectromechanical systems. *Review of Scientific Instruments*, 76(6), 2005.
- [36] A. Maali, C. Hurth, R. Boisgard, C. Jai, T. Cohen-Bouhacina, and J. Aime. Hydrodynamics of oscillating atomic force microscopy cantilevers in viscous fluids. *J. Appl. Phys.*, 97:074907, 2005.



- [37] T. Braun, V. Barwich, M.K. Ghatkesar, A.H. Bredekamp, C. Gerber, M. Hegner, and H.P. Lang. Micromechanical mass sensors for biomolecular detection in a physiological environment. *Phys. Rev. E*, 72:031907, 2005.
- [38] M.K. Ghatkesar, T. Braun, V. Barwich, J. Ramseyer, C. Gerber, M. Hegner, and H. P. Lang. Resonating modes of vibrating microcantilevers in liquid. *Appl. Phys. Lett.*, 92:043106, 2008.
- [39] J. Tamayo, A.D.L. Humphris, R.J. Owen, and M.J. Miles. High- $q$  dynamic force microscopy in liquid and its applications to living cells. *Biophys. J.*, 81, 526–537 2001.
- [40] L. Sekaric, M. Zalalutdinov, R.B. Bhiladvala, A.T. Zehnder, J.M. Parpia, and H.G. Craighead. Operation of nanomechanical resonant structures in air. *Appl. Phys. Lett.*, 81(14):2641–2643, 2002.
- [41] T. P. Burg, M. Godin, S. M. Knudsen, W. Shen, G. Carlson, J. S. Foster, K. Babcock, and S. R. Manalis. Weighing of biomolecules, single cells and single nanoparticles in fluid. *Nature Lett.*, 446:1066–1069, 2007.
- [42] M. R. Paul and J. E. Solomon. *Nanodevices for Life Sciences*, volume 4, chapter The physics and modeling of BioNEMS. Wiley-VCH, 2005.
- [43] M. T. Clark and M. R. Paul. The stochastic dynamics of an array of atomic force microscopes in a viscous fluid. *Int. J. Nonlin. Mech.*, 42:690–696, 2007.
- [44] C.A. Van Eysden and J. E. Sader. Small amplitude oscillations of a flexible thin blade in a viscous fluid: Exact analytical solution. *Phys. Fluids*, 18:123102, 2006.
- [45] R. J. Clarke, O. E. Jensen, J. Billingham, and P. M. Williams. Three-dimensional flow due to a microcantilever oscillating near a wall: an unsteady slender-body analysis. *Proc. R. Soc. A*, 462:913–933, 2006.
- [46] L. Rosenhead. *Laminar Boundary Layers*. Oxford University Press, 1963.